Research Paper
Computational Methods for Differential Equations
http://cmde.tabrizu.ac.ir
Vol. *, No. *, *, pp. 1-28
DOI:10.22034/cmde.2026.70864.3544

Investigating nonlinear dynamics and the optical soliton structures in the Spin Hirota-Maxwell-Bloch Equation for Erbium-Doped Fiber

Md. Nur Alam[1,2,3,*], Shams Forruque Ahmed[4,5,*], Cemil Tunç[6,*], and Hammad Alotaibi[7]

[1]School of Mathematical Sciences, Sunway University, Bandar Sunway, Petaling Jaya 47500, Selangor Darul Ehsan, Malaysia.

[2]Department of Mathematics, Pabna University of Science and Technology, Pabna-6600, Bangladesh.

[3]Department of Mathematics, Saveetha School of Engineering, Saveetha Institute of Medical and Technical Sciences, Chennai 602105, Tamilnadu, India.

[4]School of Mathematical Sciences, Sunway University, Bandar Sunway, Petaling Jaya 47500, Selangor Darul Ehsan, Malaysia.

[5]Miyan Research Institute, International University of Business Agriculture and Technology, Dhaka 1230, Bangladesh.

[6]School of Engineering and Natural Sciences, Istanbul Medipol University, 34810, Istanbul, Turkey.

[7]Department of Mathematics and Statistics, College of Science, Taif University, P.O. Box 11099, Taif, 21944, Saudi Arabia.

Abstract

The integrable reduced spin Hirota-Maxwell-Bloch (rsHMB) equation is an important nonlinear equation, which models the femtosecond pulse propagation in spin-field coupling, erbium-doped fibre, fibre optic technologies, and magnetisation reversal effects. Despite its general applicability, a careful analytical study of the dynamical behaviour of the rsHMB equation, including bifurcation structures, chaotic evolution, and sensitivity to initial perturbations, remains lacking. To fill this gap, this paper obtains correct soliton solutions and examines the nonlinear dynamics of the equation of rsHMB. The bifurcation and sensitivity analysis of a dynamical system is used to study periodic, quasiperiodic, and chaotic behaviours. The Runge-Kutta technique is utilized to determine the stability of the system under minimal perturbations, and the modified extended tanh technique (METF) is used to obtain various types of soliton solutions. Anti-kink, v-shaped, and compact on waves are all examples of soliton structures that can be represented in various graphical displays, such as 2D, 3D, contour, density, and modeling profiles before rotation, as well as 3D rotating surfaces. The findings affirm the nonlinear complexity of the system's nonlinear behaviour, exhibiting elastic soliton collisions, amplitude modulation, and energy conservation. The findings are part of the theoretical knowledge of ultrafast pulse propagation in erbium-doped fibres and provide valuable data for the improvement of biological imaging, optical communication, and magnetic data storage. This work will contribute to the development of nonlinear dynamical modeling and soliton-based applications in recent photonic technology and nonlinear science studies to a large extent.

Keywords. Hirota–Maxwell–Bloch equation, Modified extended tanh function method, Exact soliton solutions, Femtosecond pulse propagation, Bifurcation and sensitivity analysis, Nonlinear dynamics, Chaotic dynamics.

1991 Mathematics Subject Classification. 35Q55, 35Q60, 78A60, 37G10, 37N05, 65P20.

1. Introduction

The nonlinear partial differential equations (NLPDEs) are being increasingly used as an important tool to describe complex phenomena in numerous fields of engineering and nonlinear sciences like computer science, thermodynamics, fiber optics, biological modeling, geophysics, plasma physics, computational fluid dynamics, data science, nonlinear dynamics, chemical engineering, nonlinear optics, artificial intelligence, laser optics, electronic engineering, and communication engineering [13, 19, 20]. To discover the applications of answers for nonlinear models, mathematicians, physicians, researchers, and scientists have established numerous procedures to examine the answers of NLPDEs by

Received: 23 December 2025; Accepted: 24 April 2026.
∗ Corresponding authors. Emails: shams.f.ahmed@gmail.com, nuralam.pstu23@gmail.com, cemtunc@yahoo.com.

neural network methods, Painleve analysis, analytic analysis, bifurcation analysis, numeric analysis, Lie symmetries analysis, chaotic analysis, qualitative analysis, and conservation laws [5, 24**?**]. In this study, we investigate the rsHMB equation, which is an integrable mathematical model that describes the propagation of femtosecond pulses in erbium-doped fibers and magnetization reversal phenomena. It is visualized graphically to understand wave behavior and the impact of parameters on pulse characteristics.

Yesmakhanova et al. [23] examined the (2 + 1)-dimensional Hirota–Maxwell–Bloch system (HMBS), which often controls the transmission of ultrashort pulses in erbium-doped fibers due to higher-order effects. In the study of the rsHMB equation, Taskeen et al. [14] used the JEFE approach to analyse and comprehend the planar dynamical system, show how it depends on physical properties like sensitivity analysis and quasiperiodicity, and offer potential soliton solutions. Xue et al. [22] explored the 1- and 2-soliton solutions using symbolic computation and the Darboux transformation to apply the extended inhomogeneous coupled HMBS. Ceesay et al. [4] investigated homoclinic breather waves, periodic lump waves, and other wave forms of the rsHMB equation using the Hirota bilinear transformation. Akram and Rahman [1] study the integrable rsHMB equation and the conformable derivative of Atangana by using the full discriminant system of polynomials and the generalised auxiliary sub-equation method which they use to form a broad selection of novel wave structures. Nonlinear dynamics is a strong technique of researching on the evolving structures and is significant in several spheres [3, 16]. The process of nonlinear dynamics was initially suggested by Liu and Li [10] to determine the dynamics of a nonlinear model. It is a method of monitoring the effect of the changes in the system variables on the major system attributes. It works especially well to study the bifurcation behaviour and derive soliton solutions that are exactly determined. The nonlinear dynamics will help the researchers to investigate the transition between unsteady and steady environment. The study is concerned with the nonlinear dynamics, such as bifurcation analysis, chaotic and quasi-periodic behaviour, sensitivity tests and new soliton solutions to the rsHMB equation [14]. We hope to create soliton solutions and planar dynamics through the METF approach of finding chaotic properties that form the physical nature of the rsHMB equation. We also identify and analyse chaos by using 2D and 3D phase portraits, surface plots, time series, sensitivity behaviours of various initial conditions, contour maps and density diagrams. The foremost intention of soliton theory, an important field of applied mathematics and mathematical physics, is to solve solitary wave solutions, flowing through a system without dissipating or losing energy, and therefore it offers a solution to a significant problem of applied mathematics. Solitons are free waves that travel at a consistent speed without losing its shape and speed [12, 15, 25]. They are known to be very common in nature, have a number of applications in nonlinear dynamics, and can also provide insight into the mechanisms of other physical phenomena, such as signal processing, fluid mechanics, plasma physics, optical communication and many others [2, 17]. In this paper, METF methodology [11] is used to find new soliton solutions to the rsHMB equation [14]. This specific model has not been addressed in previous investigations using these approaches. The METF approach is an influential and well-organised instrument for explaining NLPDEs, presenting adaptability, enhanced flexibility, a broad solution space, reduced computational complexity, and enhanced flexibility to numerous physical frameworks and boundary conditions across various systematic and engineering disciplines. The blood flow under complex physiological conditions has been numerically investigated in a number of studies using various computational methods. Haider et al. [6] compared finite volume and finite element algorithms to model blood flow in two or more stenosed arteries to show the validity of hybrid numerical models in forecasting the main hemodynamic variables. In an elliptic duct, Haider and Ahmad [7] modelled Rabinowitsch fluid flow through the finite volume approach and found that rheological parameters had a greater effect, but the geometry was not realistic. Using Multiphysics effects, Haider et al. [8] investigated the magnetohydrodynamic flow of blood using hybrid nanofluids, and they compared their results with numeric which indicated that magnetic fields have a strong influence on the flow and thermal behaviour. Most recently, the finite difference method was used to investigate electroosmotic flow and heat transfer in tapered stenotic arteries [9], which found that electro-thermal effects have a combined effect on velocity and temperature distribution. Nonetheless, comparison and extensive modelling with realistic stenosed geometry and strong numerical treatment is limited. It is with this discrepancy that this paper seeks to come up with a better numerical model to improve physical meaning and biomedical use. Recent progress has shown that neural network-based analytical tools are effective in the solution of nonlinear equations, as well as in resolving such equations that have a fractional partial derivative. The method of the fractional sub-equation neural networks (fSENNs) proposed by Wang et al. [18] to

derive the precise solutions of the space-time fractional PDEs had a high ability to solve the fractional operators with great precision. Zhang and Bilige [26] earlier on suggested the bilinear method of neural network in deriving the exact solution of nonlinear evolution equations, and this became the basis of creating a relationship between bilinear forms and neural learning structures. The concept was also expanded to bilinear residual networks [28], which enhanced the stability and explicitness of solutions. In more recent work, neurosymbolic and symbolic neural methods have been created to improve interpretability and multi-modal reasoning in nonlinear models as illustrated in the case of the BLMP equation[27] and the KdV equation [21]. Nevertheless, in spite of these developments, the majority of the extant research concentrates on benchmark equations and does not have coherent frameworks that combine fractional operators, bilinear structures, and symbolic reasoning. Driven by this gap, the current research will attempt to create a more robust neural-assisted methodology of analysis, which can provide better accuracy, interpretability, and wider applicability to more nonlinear and fractional PDEs, potentially being extended to more complex physical models. The main conclusion of the current investigation is to establish the exact solution of the rsHMB equation because the solutions can provide mathematical instruments to comprehend the wave behaviour and can be used in its practical use in many ways. We study the equation of rsHMB by a dynamical system paradigm with focus on bifurcation analysis, sensitivity testing, and chaotic and quasiperiodic behaviour. Using chaos theory, we demonstrate how the transformed dynamical system behaves chaotically. By conducting a sensitivity analysis employing the Runge-Kutta method, the stability of the solution is illustrated against slight modifications in the initial conditions. Our findings demonstrate that the governing nonlinear problem exhibits periodic, quasiperiodic, and chaotic behaviours, among other features. It helps understand and control femtosecond pulses in fibre lasers, enabling faster and more reliable fibre optic communication systems. This information also supports advances in medical imaging, safe data transfer, and magnetic storage. Thus, studying rsHMB links mathematical theory to developments that enhance everyday living. We also obtain optical soliton solutions for the rsHMB problem using the METF technique. By modelling profile before revolution shapes, 3D revolving shapes, 3D shapes, contour shapes, density shapes, and 2D graphs of these generated solitons, we investigated the influence of the waves on nonlinear terms. Using visual examples, we thoroughly analyse a range of soliton structures, such as V-shaped solitons, peakons, singular solitons, singular kinks, quasiperiodic structures, and periodic structures, to demonstrate their physical behaviour in nonlinear wave propagation through media such as fluid dynamics, oceanography, coastal engineering, optical fibres, and fluids. The efficacy, efficiency, and conciseness of the present methods improve our comprehension of this model and point to wider uses in nonlinear system research. This study advances our understanding of nonlinear dynamics, including waveform features, bifurcation analysis, sensitivity, and stability, while also shedding light on dynamic elements and wave patterns. The soliton elastic collisions are graphically represented and discussed, and some important soliton physical properties, including wave velocity, amplitude, and energy, are analysed both graphically and asymptotically. The consequences and features covered in this paper may simplify our understanding of the transmission of optical solitons in erbium-doped fibre. The new solitary wave structures, profile before revolution shapes, 3D revolving shapes analysis, sensitivity analysis, and bifurcation analysis of this discovery will significantly influence nonlinear science. We also study the stability and equilibrium positions of the applicable 2D dynamical structure by understanding the bifurcation theory. Using phase-plane analysis, bifurcations and chaotic behaviours are analysed, demonstrating significant qualitative variations in the accompanying dynamical structures. This study has better understood complex nonlinear processes by examining quasiperiodic and chaotic wave patterns affected by external forces.

2. Problem formulation

In this study, we consider an integrable rsHMB system in the following form [14]:

$$\begin{cases} \frac{1}{2}\frac{\partial^2 p}{\partial x \partial t} - i\omega\frac{\partial p}{\partial t} - 2pq = 0, \\ \delta\left(\frac{\partial |p|}{\partial t}\right)^2 + \frac{\partial q}{\partial x} = 0, \end{cases} \tag{2.1}$$

The terms used in Eq. (2.1) are described below:

- $p(x,t)$: The transmission of femtosecond pulses in an erbium-doped fibre is represented by a complicated function, p, which is differentiable according to time t and a spatial variable x;

- ω and δ: ω and δ are real constants;
- $q(x,t)$: The degree of population inversion is represented in the actual differentiable function q, which corresponds to the complex envelope of the modulated waves;
- $|p|$: $|p|$ represents the modulus of p.

The Galilean transformation, a key idea in classical physics, connects the coordinates of two inertial reference frames and works especially effectively when the relative velocity between them is significantly less than the speed of light. This transformation can be widely applied to physical structures that are not relativistic. In this scenario, we use the corresponding wave transformation:

$$p(x,t) = P(\gamma)e^{i\gamma}, \quad q(x,t) = Q(\vartheta), \tag{2.2}$$

where

$$\vartheta = A(x + Bt), \qquad \gamma = Cx - Dt.$$

Substituting Eq. (2.2) into Eq. (2.1), we obtain:

$$\frac{1}{2}A^2BP'' + \frac{1}{2}iABCP' - iAB\omega P' - \frac{1}{2}iADP' + \frac{1}{2}CDP - D\omega P - 2PQ = 0, \tag{2.3}$$

$$2AB\delta PP' + 2AQ' = 0. \tag{2.4}$$

Real part is obtained as

$$A^2BP'' + 2B\delta P^3 + CDP - 2D\omega P = 0. \tag{2.5}$$

Imaginary part is

$$ABCP' - 2AB\omega P' - ADP' = 0. \tag{2.6}$$

From Eq. (2.6) of the imaginary terms, we explore the constraint conditions as:

$$C = \frac{2B\omega + D}{B}, \qquad Q = -\frac{B\delta}{2}P^2. \tag{2.7}$$

3. Investigating dynamic behaviours in the Erbium-Doped fiber model

Eq. (2.6) can be written as dynamical system of the following:

$$\begin{cases} \frac{dP(\gamma)}{d\gamma} = R, \\ \frac{dR(\gamma)}{d\gamma} = -L_1P - L_2P^3, \end{cases} \tag{3.1}$$

where $L_1 = \frac{CD-2D\omega}{A^2B}$, $\quad L_2 = \frac{2B\delta}{A^2B}$, $\quad A, B \neq 0$.

3.1. Bifurcation analysis in the Erbium-Doped fiber model.

One such mathematical technique for examining how a system's topological or qualitative structure changes as a parameter is changed is bifurcation analysis. This approach can be particularly beneficial when researching dynamical systems, as it enables one to understand more simply how stable equilibria, periodic orbits, or other invariant sets change when system parameters are updated. In order to simplify the analysis of bifurcation, we state that above equation. The corresponding Hamiltonian is (3.1), and its corresponding Hamiltonian function is as follows:

$$H(P,R) = \frac{R^2}{2} - \frac{L_1}{2}P^2 - \frac{L_2}{4}P^4 = \Psi, \tag{3.2}$$

where Ψ is a constant representing the total energy of the system. To find the equilibrium points, we solve the following system

$$\begin{cases} R = 0, \\ -L_1P - L_2P^3 = 0, \end{cases} \tag{3.3}$$

The dynamic structure expressed by Eq. (3.1) is examined in the framework of its equilibrium points and their connection with the physical boundary conditions. The functions $Y(\Phi)$, which satisfies Eq. (3.1) is supposed to

converge to the limits $\lim_{\Phi\to-\infty} Y(\Phi) = r_1$, and $\lim_{\Phi\to+\infty} Y(\Phi) = r_2$, where r_1 and r_2 are arbitrary constants. Finding the equilibrium structure (3.3) exposes three possible circumstances for the equilibrium points. If $r_1 = r_2$, the answer $Y(\Phi)$ represents a homoclinic trajectory equivalent to a solitary wave for the structure. When $r_1 \neq r_2$, $Y(\Phi)$ forms a heteroclinic orbit. For $r_1 > r_2$, $Y(\Phi)$ displays a kink wave, whereas for $r_1 < r_2$, $Y(\Phi)$ outcomes in an anti-kink wave. Furthermore, when the phase portrait of Eq. (3.1) is closed, the structure displays periodic behaviour equivalent to oscillatory answers in the physical domain. These outcomes determine how the boundary conditions r_1 and r_2 exhibit the nature of the equilibrium and the complete dynamics of the structure The equilibrium points $(\mathcal{E}_i)$ of structure (3.3) are solved as: $\mathcal{E}_1 = (0,0)$, $\mathcal{E}_2 = \left(\sqrt{\frac{-L_1}{L_2}}, 0\right)$, $\mathcal{E}_3 = \left(-\sqrt{\frac{-L_1}{L_2}}, 0\right)$.

The stability of these equilibrium points is calculated by using the Jacobian matrix of the structure:

$$J(P,R) = \begin{vmatrix} 0 & 1 \\ -L_1 - 3L_2P^2 & 0 \end{vmatrix} = L_1 + 3L_2P^2.$$

The determinant's sign influences how the equilibrium points are classified. It is possible to examine the dynamic behaviour of the structure in various regimes by changing the parameters L_1 and L_2.

Case 1. For the case $L_1 > 0$ and $L_2 > 0$, conveying precise values to the parameters $A = 2$, $B = -1$, $C = 2$, $D = 2$, $\omega = 2$, and $\delta = 2$, we obtain $L_1 = 1$, $L_2 = 1$. The system has only one equilibrium point $\mathcal{E}_1 = (0,0)$.For $\det(J(0,0)) < 0$, the equilibrium point $\mathcal{E}_1$ is classified as a center point, as illustrated in Figure 1.

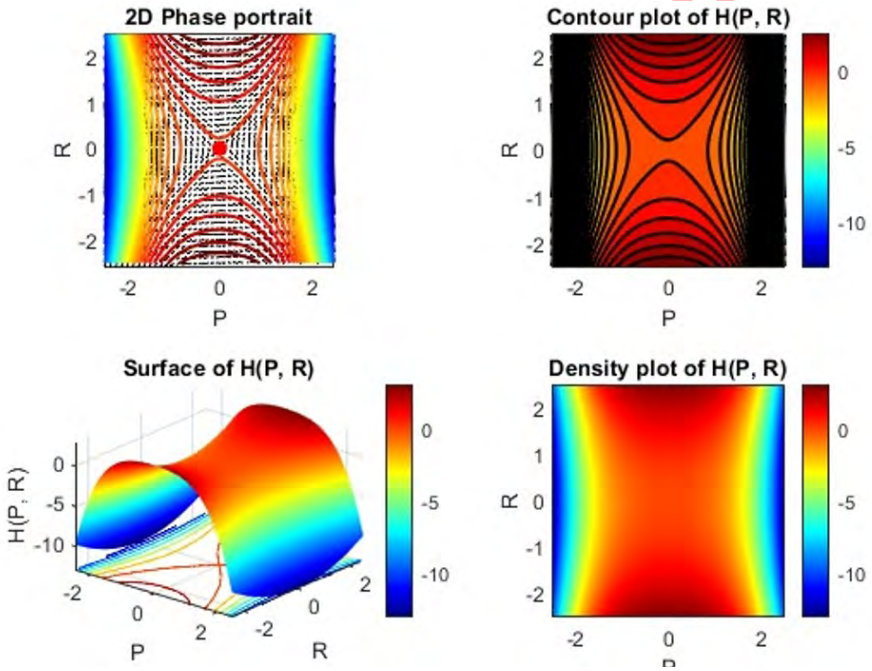

Figure 1. Phase plane analysis of system (3.1) for $a_1 > 0$ and $a_2 > 0$.

Case 2. When $L_1 < 0$ and $L_2 < 0$, taking the parameter values $A = 2$, $B = 1$, $C = 2$, $D = 2$, $\omega = 2$, and $\delta = -2$, we obtain

$$L_1 = -1, \qquad L_2 = -1.$$

The system has only one equilibrium point, $\mathcal{E}_1 = (0,0)$. Since $\det(J(0,0)) > 0$, the equilibrium point $\mathcal{E}_1$ is a saddle point, as illustrated in Figure 2.

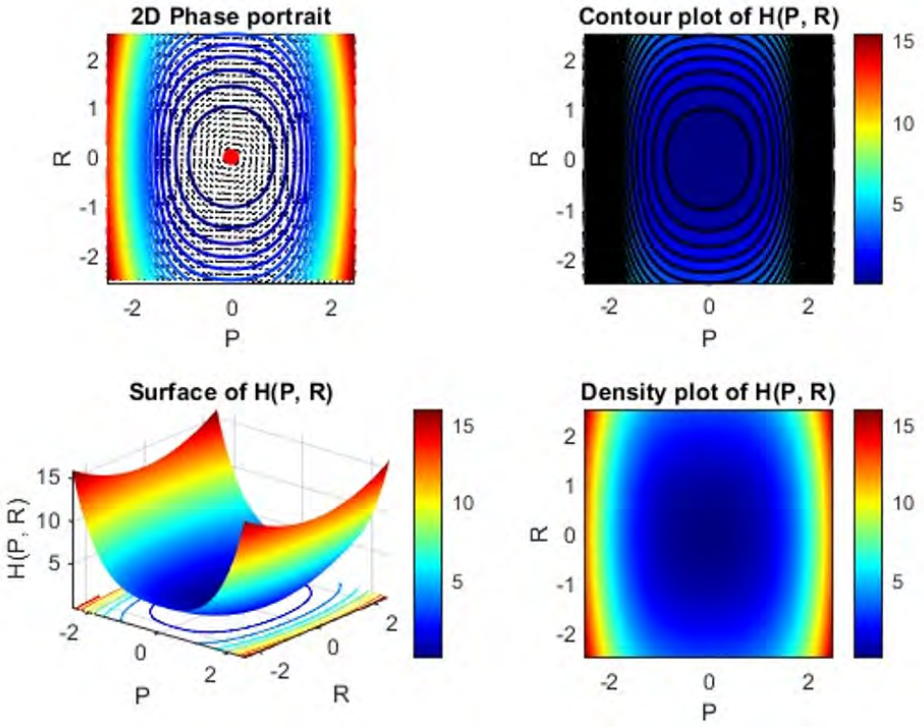

Figure 2. Phase plane analysis of system (3.1) for $a_1 < 0$ and $a_2 < 0$.

Case 3. If we choose $L_1 < 0$ and $L_2 > 0$, conveying precise values to the parameters $A = 2$, $B = 1$, $C = 2$, $D = 2$, $\omega = 2$, and $\delta = 2$, we obtain $L_1 = -1$, $L_2 = 1$.The system has three equilibrium points: $\mathcal{E}_1 = (0, 0)$, $\mathcal{E}_2 = (1, 0)$, $\mathcal{E}_3 = (-1, 0)$. For $\det(J(0, 0)) > 0$, the equilibrium point $\mathcal{E}_1 = (0, 0)$ is classified as a saddle point. Similarly, $J(\sqrt{-1}, 0) < 0$, the equilibrium point $\mathcal{E}_2 = (1, 0)$ is identified as a center point. Finally, $J(-\sqrt{1}, 0) < 0$, the equilibrium point $\mathcal{E}_3 = (-\sqrt{1}, 0)$ identified as a center point as illustrated in the following Figure 3.

Case 4. If we choose $L_1 > 0$ and $L_2 < 0$, conveying precise values to the parameters $A = 2$, $B = 1$, $C = 2$, $D = 2$, $\omega = 2$, and $\delta = -2$, we obtain $L_1 = -1$, $L_2 = 1$.The system has three equilibrium points: $\mathcal{E}_1 = (0, 0)$, $\mathcal{E}_2 = (\sqrt{1}, 0)$, $\mathcal{E}_3 = (-\sqrt{1}, 0)$. For $\det(J(0, 0)) > 0$, the equilibrium point $\mathcal{E}_1 = (0, 0)$ is classified as a center point. Similarly, $J(\sqrt{-1}, 0) < 0$, the equilibrium point $\mathcal{E}_2 = (1, 0)$ is identified as a saddle point. Finally, $J(-\sqrt{1}, 0) < 0$, the equilibrium point $\mathcal{E}_3 = (-\sqrt{1}, 0)$ identified as a saddle point as illustrated in the following Figure 4.

Case 5. Bifurcation Diagram of the System (L_1 vs L_2): In the parameter plane, the diagram visualizes how the number of real equilibrium points of the system varies depending on the values of the parameters L_1 and L_2. The orange regions represent parameter combinations where the system has a single real equilibrium point at $(\Phi, \Psi) = (0, 0)$ and the blue regions correspond to combinations where the system admits three real equilibria, located at $(\Phi, \Psi) = (0, 0)$, $(\Phi, \Psi) = \left(\pm\sqrt{\frac{-L_1}{L_2}}, 0\right)$, which occur when $\frac{L_1}{L_2} < 0$. And the black dashed lines indicate the bifurcation curves (here, it's a line) at $L_1 = 0$ and $L_2 = 0$, where a qualitative change in the number of equilibria occurs. These lines form the bifurcation set, separating regions with different dynamical behavior. If we choose any point in the (L_1, L_2)-plane and move this point in any direction, whenever it crosses the black dashed line, bifurcation (Change of number of equilibrium point(s)) occurs. L_1 versus L_2 are plotted in Figure 5, which presents the regions where the fixed points are saddles or centers. The bifurcation point (i.e., in which value a center becomes a saddle or vice versa) is identified in the figure below.

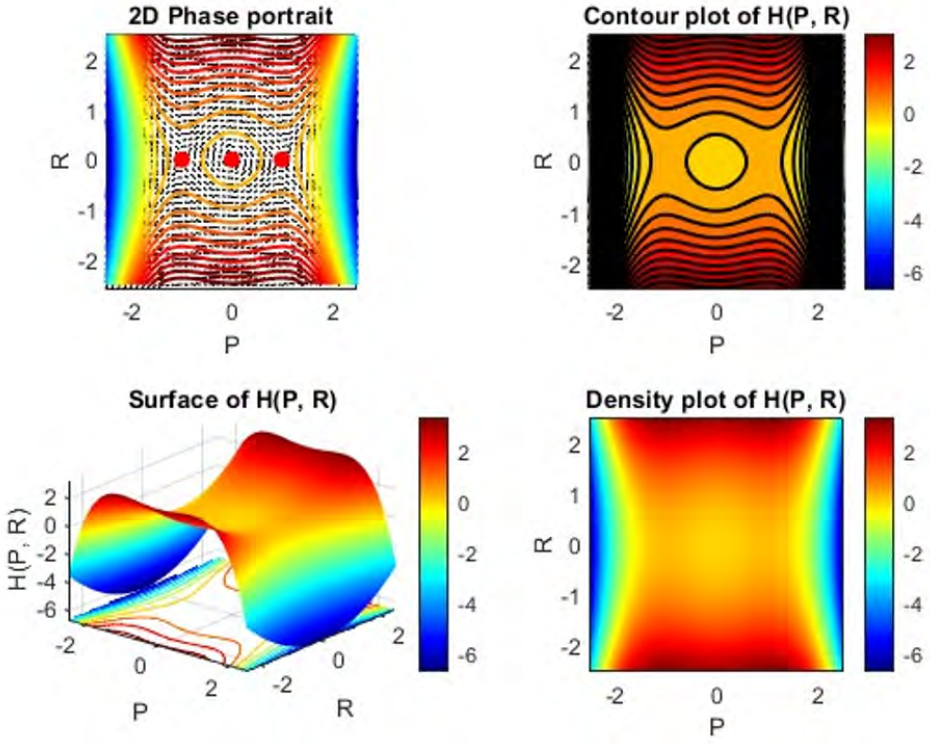

Figure 3. Phase plane analysis of system (3.1) for $a_1 < 0$ and $a_2 > 0$.

3.2. **Chaotic and quasi-periodic behaviour of the governing model with a perturbation term.** Next, we will examine the chaotic behaviour of the concatenated model. Investigating chaotic systems is often assisted by time series and phase visualisations. Bifurcations in nonlinear models may result in several dynamics, including chaotic behaviour. In the previous section, we observed that Eq. (3.1) for the planar dynamical construct does not display chaotic features; nevertheless, when an external disturbance comes into play, it does. To assess the extent to which the system exhibits periodic solutions and chaotic behaviour, we introduce a perturbed system that incorporates ongoing external influences as described in Eq. (3.1):

$$\begin{cases} \frac{dP(\gamma)}{d\gamma} = R, \\ \frac{dR(\gamma)}{d\gamma} = -L_1 P - L_2 P^3 + \Psi(\gamma), \end{cases} \tag{3.4}$$

where $\Psi(\gamma)$ represents the perturbation term. The perturbation terms with various parameters discussed below can be utilised to explore quasi-periodic and chaotic behaviour in connection with phase portraits and multistability. It is observed that chaotic waves are extremely sensitive to beginning values and display irregular, non-repeating structures. The quasi-periodic waves, on the other hand, have complicated but predictable structures that are not exactly repetitive and frequently occur in related oscillators or systems with several degrees of freedom. Some excellent visual aids will be employed to get there, including time series plots, 2D phase portraits, and 3D phase portraits. The wave patterns are similar to many natural phenomena such as ocean waves, climate models, optics, telecommunications, plasma physics and the biological cycles.

Considering the perturbation term $\Psi(\gamma) = b\cos(\eta\gamma)$ in Eq. (3.4), an external periodic force of frequency η and strength b is applied to the system via the perturbation term $\Psi(\gamma) = b\cos(\eta\gamma)$. The investigation of the values of different physical parameters allows an individual to identify the transformational dynamics of the system. This paper looks at the impact of varying b and η when the other parameters are held constant. These reasons are important in

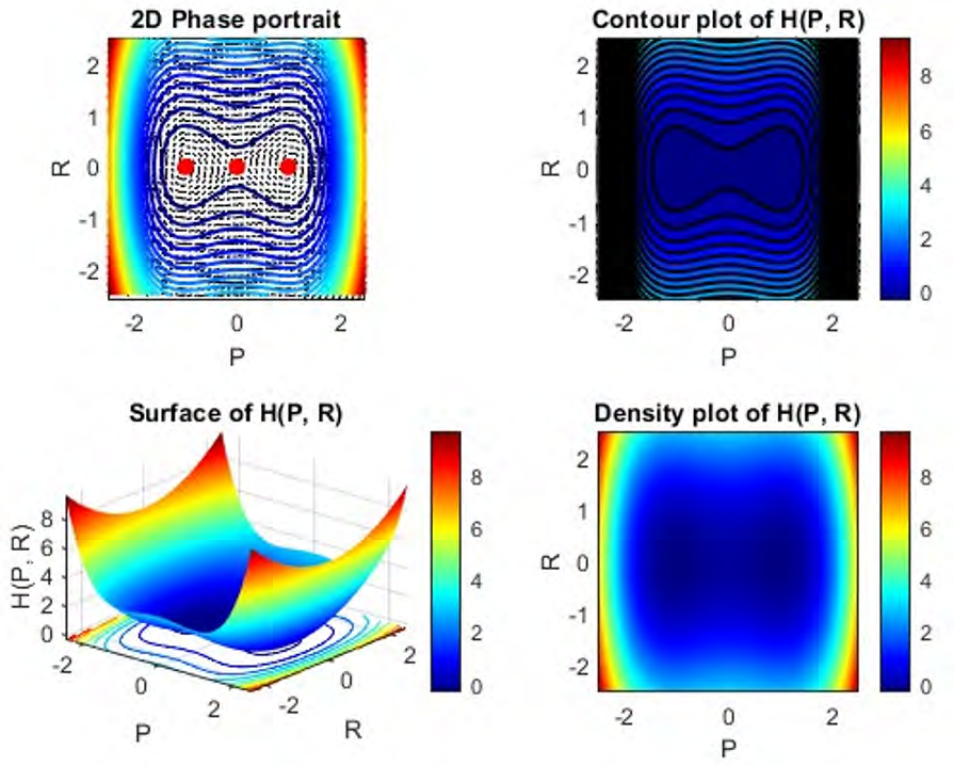

Figure 4. Phase plane analysis of system (3.1) for $a_1 < 0$ and $a_2 > 0$.

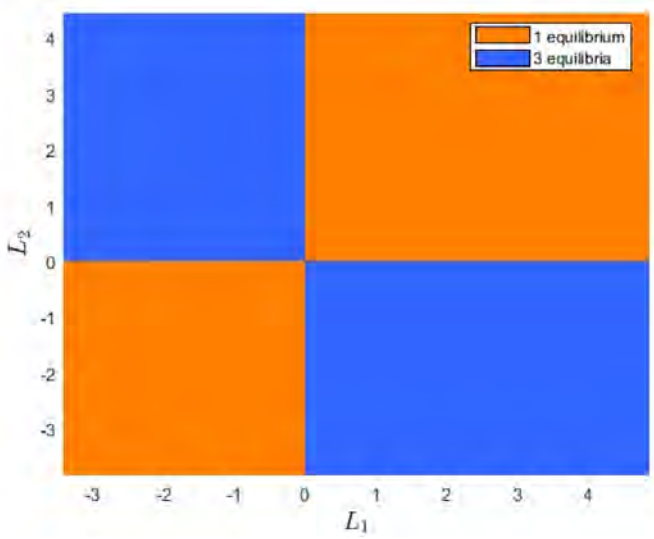

Figure 5. Bifurcation diagram of the system (3.1) with two parameters L_1 vs L_2.

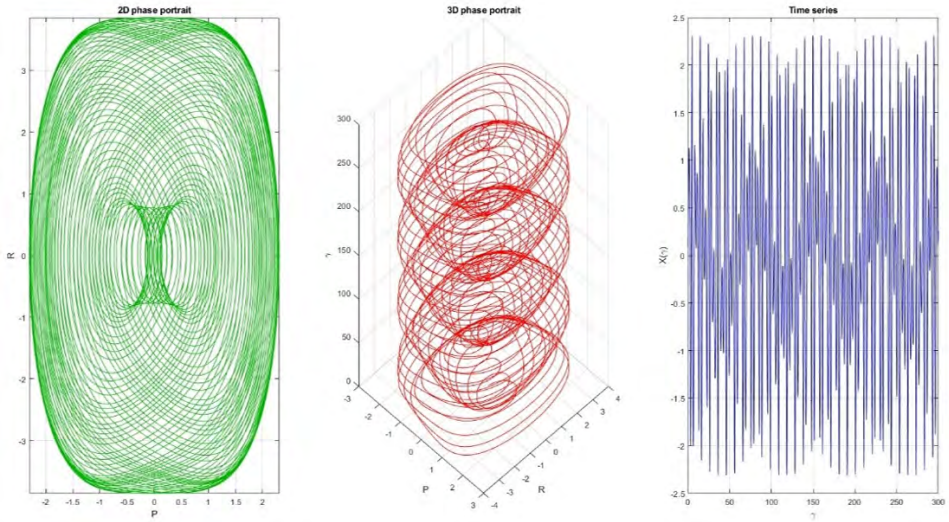

Figure 6. Dynamical behaviour of the perturbed system (3.4) for $L_1 = 1$, $L_2 = 1$, $b = 1.8$, $\eta = 1.3$.

that they can give rise to the complex behaviours, such as between the regular to chaotic states, and are very important on the stability of the system. The knowledge of these transitions aids in the setting of plans of how to manage or exploit chaotic dynamics and in the forecasting of system responses in diverse conditions. The chaotic behaviour is represented by a number of illustrations that play an important role in comprehending and visualising the dynamics of the complex systems. These are: time series plots, which follow the history of variables over time; 3D phase portraits, which follow intricate phase space dynamics; and 2D plots, which follow simple behaviour patterns. This is critical as a symbolic factor of the delicate nature of the chaotic systems that a minor shift in the initial conditions or parameters might drastically affect the trajectory of the system. an external periodic force with amplitude b and frequency η is applied to the system. We display a 2D phase portrait, a 3D phase portrait, and the time series of the chaotic behaviour for Eq. (3.4) with $b = 1.5$ and $\eta = 3$, which is shown in Figure 6.

Assuming $\Psi(\gamma) = b\sin(\eta\gamma)$ in Eq. (3.4), Figure 7 shows chaotic behaviours (2D phase portrait, a 3D phase portrait, and the time series) for the values of $L_1 = 1$, $L_2 = 1$, $b = 1.8$, $\eta = 1.3$.

Considering $\Psi(\gamma) = b\tan(\eta\gamma)$ in Eq. (3.4), Figure 8 shows chaotic behaviours (2D phase portrait, a 3D phase portrait, and the time series) for the values of $L_1 = 1$, $L_2 = 1$, $b = 1.8$, $\eta = 0.002$.

The following Gaussian function is considered as a perturbation term. Considering $\Psi(\gamma) = b\exp\left(-\frac{(\eta\gamma)^2}{2}\right)$, where $b = \frac{90}{\sqrt{2\pi}}$, $\eta = 0.12$ in Eq. (3.4), Figure 9 presents the 2D and 3D phase portraits along with the time series of the system (3.4), demonstrating that the system is quasi-periodic, as indicated by the periodic irregularity of the wave. The system (3.4) operates chaotically, whereas the external force's amplitude and frequency are minimal, but under some circumstances, it transitions to more stable dynamics.

Assume $\Psi(\gamma) = \cosh(0.023\gamma)$ in Eq. (3.4). Figure 10 presents the 2D and 3D phase portraits along with the time series of the system (3.4), demonstrating that the system is quasi-periodic, characterised by complex oscillations that, as indicated by the periodic irregularity of the wave. The system (3.4) operates chaotically, while the amplitude and frequency of the external force are minimal; however, under certain circumstances, it can transition to more unstable dynamics.

Considering $\Psi(\gamma) = \sinh(0.023\gamma)$ in Eq. (3.4), Figure 11 illustrates the chaotic dynamics through 2D/3D phase portraits and the time series for $L_1 = 1$, $L_2 = 1$, $b = 0.023$, $\eta = 0.023$.

Considering $\Psi(\gamma) = \tanh(0.023\gamma)$ in Eq. (3.4), Figure 12 shows chaotic behaviours (2D phase portrait, a 3D phase portrait, and the time series) for the values of $L_1 = 1$, $L_2 = 1$, $b = 1.8$, $\eta = 0.002$.

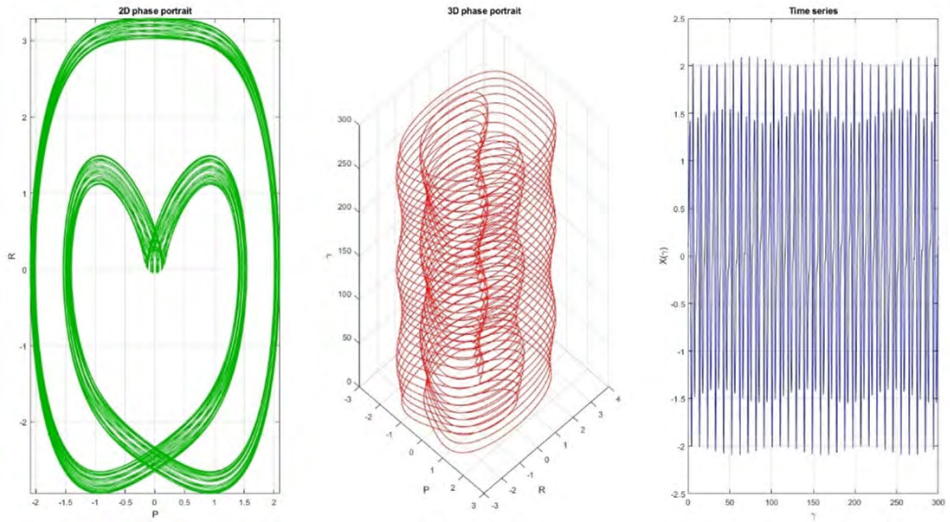

Figure 7. Dynamical behaviour of the perturbed system (3.4) for $L_1 = 1$, $L_2 = 1$, $b = 1.8$, $\eta = 1.3$.

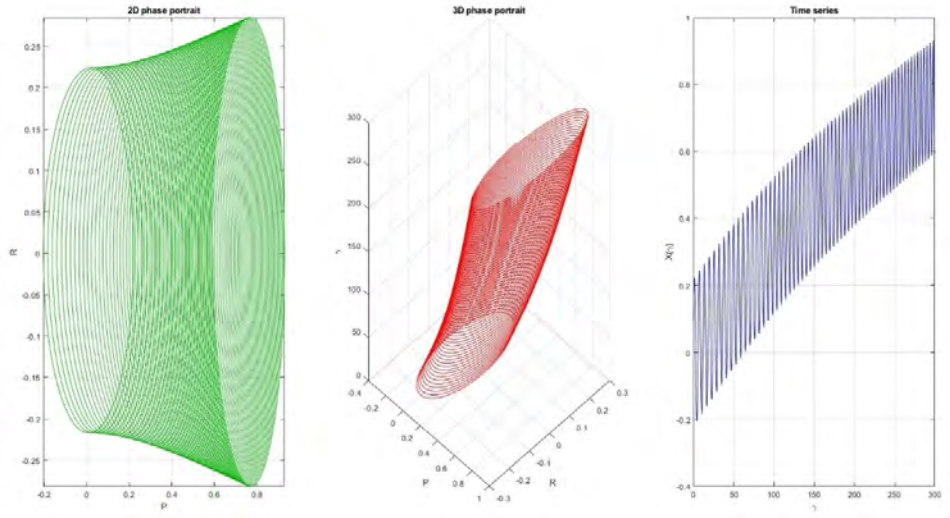

Figure 8. Dynamical behaviour of the perturbed system (3.4) for $L_1 = 1$, $L_2 = 1$, $b = 1.8$, $\eta = 0.002$.

Based on the summary above, we observe that as the perturbed wave frequency increases, the periodic waves first transition to quasi-periodic and finally to chaotic wave patterns. As a result, the model shows chaotic and quasi-periodic behaviour when influenced by outside forces, which is important for understanding, predicting, and controlling complex dynamic systems.

3.3. **Sensitivity tests in the Erbium-Doped Fibre model.** In this section, we investigate the sensitivity of the dynamical system expressed in (3.1) using the widely used and effective Runge-Kutta method. The parameters have been set with the following values: $A = 2$, $B = -1$, $C = 2$, $D = 2$, $\omega = 2$, $\delta = 2$, we obtain $L_1 = 1$, $L_2 = 1$ of the system (3.1). The initial conditions for the system (3.1) are as given below:

$$P(0) = 0.1, \quad R(0) = 0.1; \quad P(0) = 0.15, \quad R(0) = 0.1; \quad P(0) = 0.2, \quad R(0) = 0.1;$$

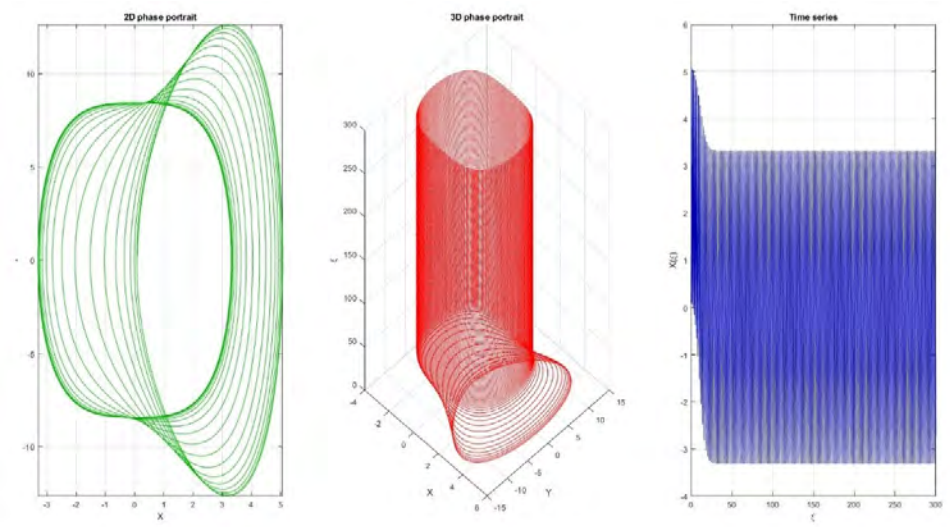

Figure 9. Dynamical behaviour of the perturbed system (3.4) for $L_1 = 1$, $L_2 = 1$, $b = \frac{90}{\sqrt{2\pi}}$, $\eta = 0.12$.

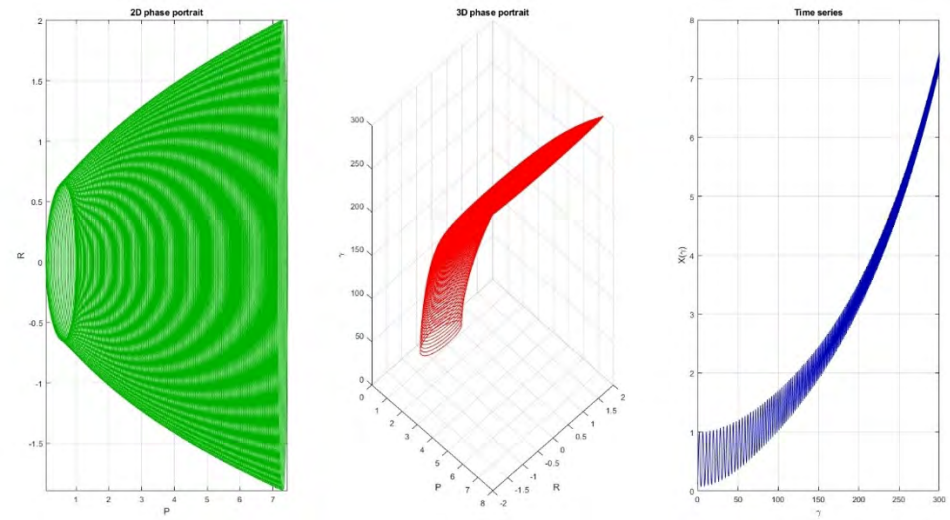

Figure 10. Dynamical behaviour of the perturbed system (3.4) for $L_1 = 1$, $L_2 = 1$, $b = 0.8$, $\eta = 0.023$.

$P(0) = 0.3, \quad R(0) = 0.1; \quad P(0) = 0.3, \quad R(0) = 0.5; \quad P(0) = 0.3, \quad R(0) = 0.9;$
$P(0) = -0.3, \quad R(0) = 0.1; \quad P(0) = -0.6, \quad R(0) = 0.2; \quad P(0) = -0.9, \quad R(0) = 0.3;$
$P(0) = -0.5, \quad R(0) = 0.5; \quad P(0) = -0.7, \quad R(0) = 0.7; \quad P(0) = -0.9, \quad R(0) = 0.9.$

We examine how the frequency term affects the system under this study. This is accomplished by defining the physical characteristics of the system being studied and discussing the effects of the disturbance force and frequency on the system. Figure 13 illustrates how the dynamical system behaves sensitively for varying initial conditions. It displays sensitive behaviour if we alter the initial conditions by changing the slit.

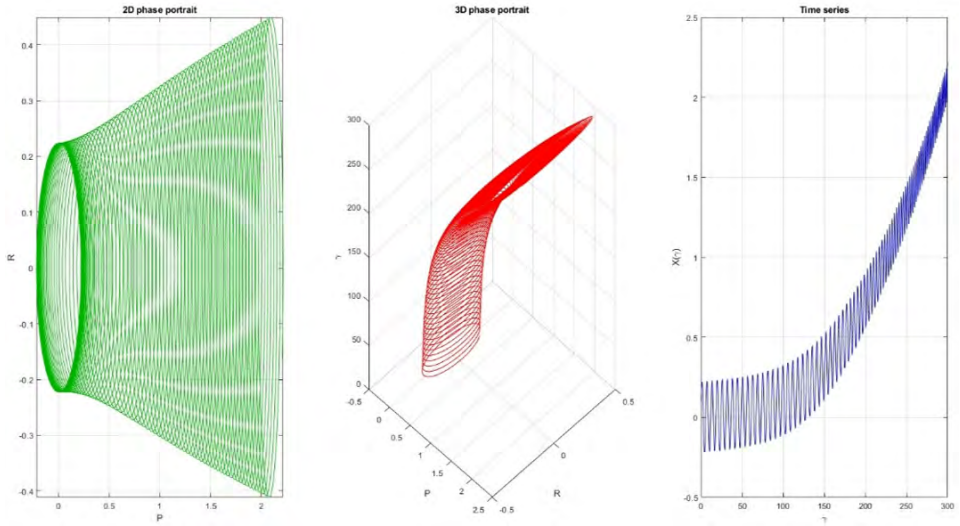

Figure 11. Dynamical behaviour of the perturbed system (3.4) for $L_1 = 1$, $L_2 = 1$, $b = 0.023$, $\eta = 0.023$.

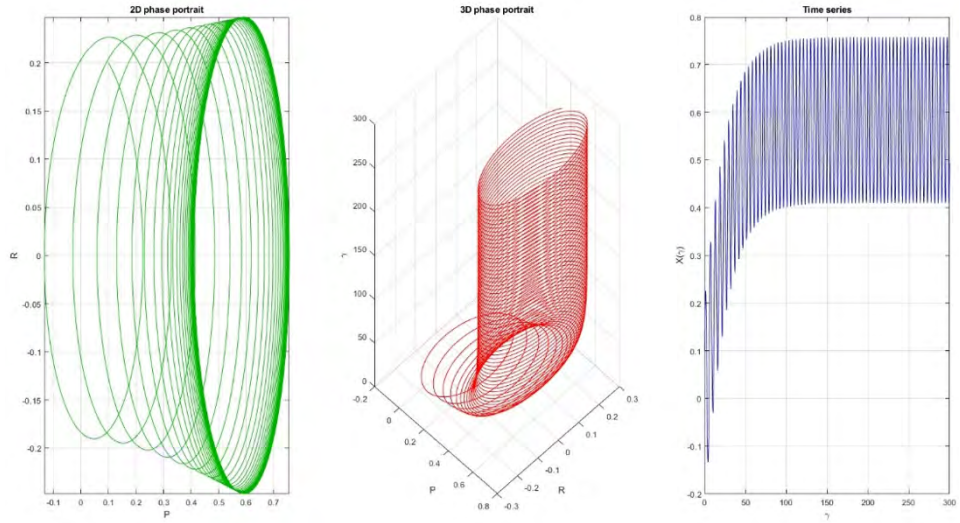

Figure 12. Dynamical behaviour of the perturbed system (3.4) for $L_1 = 1$, $L_2 = 1$, $b = 0.8$, $\eta = 0.023$.

4. Methodology, application, and graphical representations

In this section, we briefly outline the method used, describe its applications, and present graphical representations of the solitons obtained from it.

4.1. The modified extended tanh function method.

We consider:

$$W\left(P, \frac{\partial P}{\partial t}, \frac{\partial P}{\partial x}, \frac{\partial^2 P}{\partial x^2}, \frac{\partial^2 P}{\partial t \partial x}, \frac{\partial^2 P}{\partial t^2}, \dots\right) = 0. \tag{4.1}$$

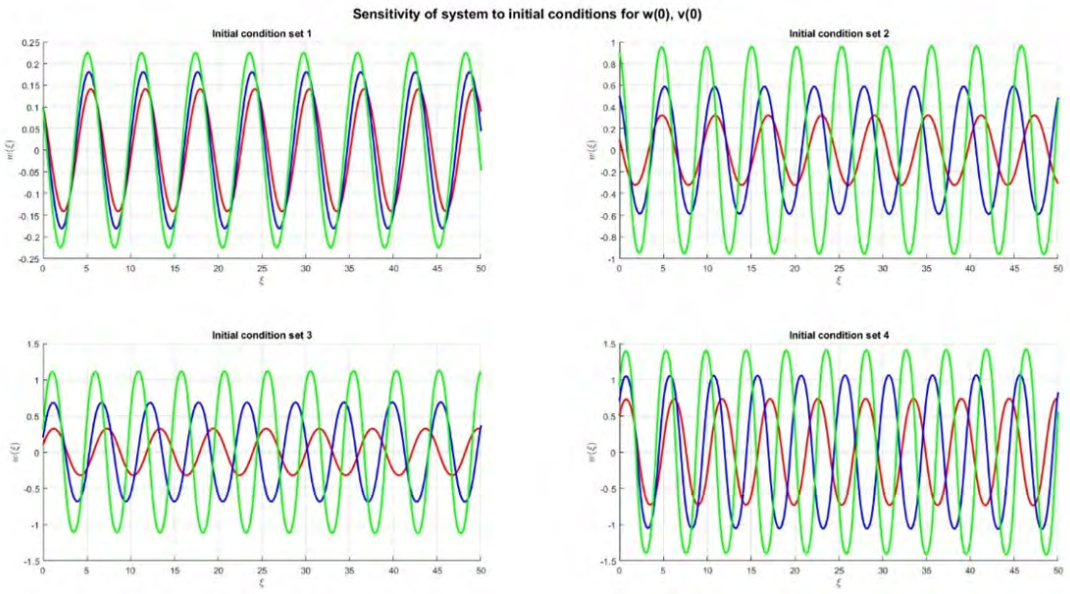

Figure 13. Sensitive behaviour of the dynamical system (3.1) for different initial conditions.
Initial condition set 1: $P(0) = 0.1$, $R(0) = 0.1$; $P(0) = 0.15$, $R(0) = 0.1$; $P(0) = 0.2$, $R(0) = 0.1$.
Initial condition set 2: $P(0) = 0.3$, $R(0) = 0.1$; $P(0) = 0.3$, $R(0) = 0.5$; $P(0) = 0.3$, $R(0) = 0.9$.
Initial condition set 3: $P(0) = -0.3$, $R(0) = 0.1$; $P(0) = -0.6$, $R(0) = 0.2$; $P(0) = -0.9$, $R(0) = 0.3$.
Initial condition set 4: $P(0) = -0.5$, $R(0) = 0.5$; $P(0) = -0.7$, $R(0) = 0.7$; $P(0) = -0.9$, $R(0) = 0.9$.

Using the travelling wave:

$$P(\gamma) = P(x,t), \qquad \gamma = x - ct, \tag{4.2}$$

Substituting Eq. (4.1) into Eq. (4.2), the following equation is obtained:

$$F\left(P, P', P'', \dots\right) = 0, \tag{4.3}$$

We consider the ansatz equation:

$$P(\gamma) = B_0 + \sum_{i=1}^{M} \left[B_i\, N(\gamma)^i + C_i\, N(\gamma)^{-i}\right]. \tag{4.4}$$

The constants B_0, B_i, and C_i must be subsequently demonstrated in a way that guarantees either B_M or C_M is not equal to zero, and $N(\gamma)$ is a function that satisfies the specified Riccati ODE:

$$N'(\gamma) = T + N(\gamma)^2. \tag{4.5}$$

The set of solutions of Eq. (4.5) is established as follows:

$$N(\gamma) = \begin{cases} -\sqrt{-T}\,\tanh\left(\sqrt{-T}\,\gamma\right), & T < 0, \\ -\sqrt{-T}\,\coth\left(\sqrt{-T}\,\gamma\right), & T < 0, \\ -\dfrac{1}{\gamma}, & T = 0, \\ \sqrt{T}\,\tan\left(\sqrt{T}\,\gamma\right), & T > 0, \\ -\sqrt{T}\,\cot\left(\sqrt{T}\,\gamma\right), & T > 0. \end{cases} \tag{4.6}$$

The phases of the METF method are outlined in an algorithm we present. The process for applying the approach to NLEEs of the following algorithm is clearly and methodically summarized by this visual aid:

(1) Start with the given PDE:

$$F(P, P_t, P_x, P_{xx}, \dots) = 0.$$

(2) Apply the travelling wave transformation:

$$P(x,t) = P(\gamma), \quad \gamma = x - vt.$$

(3) Reduce the PDE to an ordinary differential equation (ODE).
(4) Expand the solution in a finite series form.
(5) Balance the highest-order nonlinear and derivative terms to determine M and solve for unknown coefficients.
(6) Substitute the obtained constants into the ansatz to construct $P(\gamma)$.
(7) Obtain exact solutions.

4.2. **Solving Optical Soliton Structures of the rsHMB System via the METF Method.** Balancing the nonlinear term P^3 with the highest derivative term P'' in Eq. (2.6) gives $M = 1$. Therefore, the solution takes the form:

$$P(\gamma) = B_0 + B_1 N(\gamma) + C_1 N^{-1}(\gamma). \tag{4.7}$$

By substituting Eq. (4.7) into the reduced equation and equating coefficients, we obtain a system of algebraic equations. Solving this system yields the following parameter sets:
Phase I.

$$E = \pm\sqrt{\frac{-1}{\delta}}, \quad B = -\frac{D(C-2\omega)}{2TA^2}, \quad U_0 = 0, \quad U_1 = 0, \quad V_1 = EAT.$$

Phase II.

$$E = \pm\sqrt{\frac{-1}{\delta}}, \quad B = -\frac{D(C-2\omega)}{2TA^2}, \quad U_0 = 0, \quad U_1 = EA, \quad V_1 = 0.$$

Phase III.

$$E = \pm\sqrt{\frac{-1}{\delta}}, \quad B = -\frac{D(C-2\omega)}{8TA^2}, \quad U_0 = 0, \quad U_1 = EA, \quad V_1 = \frac{AT}{E\delta}.$$

Phase IV.

$$E = \pm\sqrt{\frac{-1}{\delta}}, \quad B = -\frac{D(C-2\omega)}{4TA^2}, \quad U_0 = 0, \quad U_1 = EA, \quad V_1 = -\frac{AT}{E\delta}.$$

By replacing the aforementioned Phase-I values in (4.7), we obtain the following relations, respectively:

$$p_{11}(x,t) = (EAT \times \{-\sqrt{-T}\tanh(\sqrt{-T}\gamma)\}^{-1}) \times e^{i\gamma}, \quad T > 0;$$

$$q_{11}(x,t) = \frac{1}{2}[(EAT \times \{-\sqrt{-T}\tanh(\sqrt{-T}\gamma)\}^{-1}) \times e^{i\gamma}]^2 \times (-B\delta), \quad T > 0;$$

$$p_{12}(x,t) = (EAT \times \{-\sqrt{-T}\coth(\sqrt{-T}\gamma)\}^{-1}) \times e^{i\gamma}, \quad T > 0;$$

$$q_{12}(x,t) = \frac{1}{2}[(EAT \times \{-\sqrt{-T}\coth(\sqrt{-T}\gamma)\}^{-1}) \times e^{i\gamma}]^2 \times (-B\delta), \quad T > 0;$$

$$p_{13}(x,t) = (EAT \times (1/\gamma)^{-1}) \times e^{i\gamma}, \quad T = 0;$$

$$q_{13}(x,t) = \frac{1}{2}[(EAT \times (1/\gamma)^{-1}) \times e^{i\gamma}]^2 \times (-B\delta), \quad T = 0;$$

$$p_{14}(x,t) = (EAT \times \{\sqrt{T}\tan(\sqrt{T}\gamma)\}^{-1}) \times e^{i\gamma}, \quad T < 0;$$

$$q_{14}(x,t) = \frac{1}{2}[(EAT \times \{\sqrt{T}\tan(\sqrt{T}\gamma)\}^{-1}) \times e^{i\gamma}]^2 \times (-B\delta), \quad T < 0;$$

$$p_{15}(x,t) = (EAT \times \{-\sqrt{T}\cot(\sqrt{T}\gamma)\}^{-1}) \times e^{i\gamma}, \quad T<0;$$
$$q_{15}(x,t) = \frac{1}{2}[(EAT \times \{-\sqrt{T}\cot(\sqrt{T}\gamma)\}^{-1}) \times e^{i\gamma}]^2 \times (-B\delta), \quad T<0.$$

By replacing the aforementioned Phase-II values in (4.7), we obtain:

$$p_{21}(x,t) = (EA \times \{-\sqrt{-T}\tanh(\sqrt{-T}\gamma)\}) \times e^{i\gamma}, \quad T>0;$$
$$q_{21}(x,t) = \frac{1}{2}[(EA \times \{-\sqrt{-T}\tanh(\sqrt{-T}\gamma)\}) \times e^{i\gamma}]^2 \times (-B\delta), \quad T>0;$$
$$p_{22}(x,t) = (EA \times \{-\sqrt{-T}\coth(\sqrt{-T}\gamma)\}) \times e^{i\gamma}, \quad T>0;$$
$$q_{22}(x,t) = \frac{1}{2}[(EA \times \{-\sqrt{-T}\coth(\sqrt{-T}\gamma)\}) \times e^{i\gamma}]^2 \times (-B\delta), \quad T>0;$$
$$p_{23}(x,t) = (EA \times (1/\gamma)) \times e^{i\gamma}, \quad T=0;$$
$$q_{23}(x,t) = \frac{1}{2}[(EA \times (1/\gamma))]^2 \times (-B\delta), \quad T>0;$$
$$p_{24}(x,t) = (EA \times \{\sqrt{T}\tan(\sqrt{T}\gamma)\}) \times e^{i\gamma}, \quad T<0;$$
$$q_{24}(x,t) = \frac{1}{2}[(EA \times \{\sqrt{T}\tan(\sqrt{T}\gamma)\}) \times e^{i\gamma}]^2 \times (-B\delta), \quad T>0;$$
$$p_{25}(x,t) = (EA \times \{-\sqrt{T}\cot(\sqrt{T}\gamma)\}) \times e^{i\gamma}, \quad T<0;$$
$$q_{25}(x,t) = \frac{1}{2}[(EA \times \{-\sqrt{T}\cot(\sqrt{T}\gamma)\}) \times e^{i\gamma}]^2 \times (-B\delta), \quad T>0.$$

By replacing the aforementioned Phase-III values in (4.7), we obtain:

$$p_{31}(x,t) = (EA \times \{-\sqrt{-T}\tanh(\sqrt{-T}\gamma)\} + AT/E\delta \times \{-\sqrt{-T}\tanh(\sqrt{-T}\gamma)\}^{-1}) \times e^{i\gamma}, \quad T>0;$$
$$q_{31}(x,t) = \frac{1}{2}[(EA \times \{-\sqrt{-T}\coth(\sqrt{-T}\gamma)\} + AT/E\delta \times \{-\sqrt{-T}\coth(\sqrt{-T}\gamma)\}^{-1}) \times e^{i\gamma}]^2 \times (-B\delta);$$
$$p_{32}(x,t) = (EA \times \{-\sqrt{-T}\coth(\sqrt{-T}\gamma)\} + AT/E\delta \times \{-\sqrt{-T}\coth(\sqrt{-T}\gamma)\}^{-1}) \times e^{i\gamma}, \quad T>0;$$
$$q_{32}(x,t) = \frac{1}{2}[(EA \times \{-\sqrt{-T}\coth(\sqrt{-T}\gamma)\} + AT/E\delta \times \{-\sqrt{-T}\coth(\sqrt{-T}\gamma)\}^{-1}) \times e^{i\gamma}]^2 \times (-B\delta);$$
$$p_{33}(x,t) = (EA \times (1/\gamma) + AT/E\delta \times (1/\gamma)^{-1}) \times e^{i\gamma}, \quad T=0;$$
$$q_{33}(x,t) = \frac{1}{2}[(EA \times (1/\gamma) + AT/E\delta \times (1/\gamma)^{-1}) \times e^{i\gamma}]^2 \times (-B\delta), \quad T>0;$$
$$p_{34}(x,t) = (EA \times \{\sqrt{T}\tan(\sqrt{T}\gamma)\} + AT/E\delta \times \{\sqrt{T}\tan(\sqrt{T}\gamma)\}^{-1}) \times e^{i\gamma}, \quad T<0;$$
$$q_{34}(x,t) = \frac{1}{2}[(EA \times \{\sqrt{T}\tan(\sqrt{T}\gamma)\} + AT/E\delta \times \{\sqrt{T}\tan(\sqrt{T}\gamma)\}^{-1}) \times e^{i\gamma}]^2 \times (-B\delta);$$
$$p_{35}(x,t) = (EA \times \{-\sqrt{T}\cot(\sqrt{T}\gamma)\} + AT/E\delta \times \{-\sqrt{T}\cot(\sqrt{T}\gamma)\}^{-1}) \times e^{i\gamma}, \quad T<0;$$
$$q_{35}(x,t) = \frac{1}{2}[(EA \times \{-\sqrt{T}\cot(\sqrt{T}\gamma)\} + AT/E\delta \times \{-\sqrt{T}\cot(\sqrt{T}\gamma)\}^{-1}) \times e^{i\gamma}]^2 \times (-B\delta).$$

By replacing the aforementioned Phase-IV values in (4.7), we obtain the following relations:

$$p_{41}(x,t) = (EA \times \{-\sqrt{-T}\tanh(\sqrt{-T}\gamma)\} - \frac{AT}{E\delta} \times \{-\sqrt{-T}\tanh(\sqrt{-T}\gamma)\}^{-1}) \times e^{i\gamma}, \quad T>0;$$
$$q_{41}(x,t) = \frac{1}{2}[(EA \times \{-\sqrt{-T}\tanh(\sqrt{-T}\gamma)\} - \frac{AT}{E\delta} \times \{-\sqrt{-T}\tanh(\sqrt{-T}\gamma)\}^{-1}) \times e^{i\gamma}]^2 \times (-B\delta);$$
$$p_{42}(x,t) = (EA \times \{-\sqrt{-T}\coth(\sqrt{-T}\gamma)\} - \frac{AT}{E\delta} \times \{-\sqrt{-T}\coth(\sqrt{-T}\gamma)\}^{-1}) \times e^{i\gamma}, \quad T>0;$$
$$q_{42}(x,t) = \frac{1}{2}[(EA \times \{-\sqrt{-T}\coth(\sqrt{-T}\gamma)\} - \frac{AT}{E\delta} \times \{-\sqrt{-T}\coth(\sqrt{-T}\gamma)\}^{-1}) \times e^{i\gamma}]^2 \times (-B\delta);$$

$$p_{43}(x,t) = (EA \times (1/\gamma) - \frac{AT}{E\delta} \times (1/\gamma)^{-1}) \times e^{i\gamma}, \quad T = 0;$$
$$q_{43}(x,t) = \frac{1}{2}[(EA \times (1/\gamma) - \frac{AT}{E\delta} \times (1/\gamma)^{-1}) \times e^{i\gamma}]^2 \times (-B\delta), \quad T > 0;$$
$$p_{44}(x,t) = (EA \times \{\sqrt{T}\tan(\sqrt{T}\gamma)\} - \frac{AT}{E\delta} \times \{\sqrt{T}\tan(\sqrt{T}\gamma)\}^{-1}) \times e^{i\gamma}, \quad T < 0;$$
$$q_{44}(x,t) = \frac{1}{2}[(EA \times \{\sqrt{T}\tan(\sqrt{T}\gamma)\} - \frac{AT}{E\delta} \times \{\sqrt{T}\tan(\sqrt{T}\gamma)\}^{-1}) \times e^{i\gamma}]^2 \times (-B\delta);$$
$$p_{45}(x,t) = (EA \times \{-\sqrt{T}\cot(\sqrt{T}\gamma)\} - \frac{AT}{E\delta} \times \{-\sqrt{T}\cot(\sqrt{T}\gamma)\}^{-1}) \times e^{i\gamma}, \quad T < 0;$$
$$q_{45}(x,t) = \frac{1}{2}[(EA \times \{-\sqrt{T}\cot(\sqrt{T}\gamma)\} - \frac{AT}{E\delta} \times \{-\sqrt{T}\cot(\sqrt{T}\gamma)\}^{-1}) \times e^{i\gamma}]^2 \times (-B\delta).$$

4.3. **Graphical Representation.** This section explains the outcomes and visually examines a few acquired responses. The METF approach has been employed to obtain the rsHMBS model's analytical outcomes. These solutions are efficiently acquired as multiple solitons, V-shaped solitons, compaction solitons, singular periodic solitons, bell-shaped solitons, anti-kink solitons, bird fly solitons, peakons, singular solitons, singular kinks, quasiperiodic structures, periodic structures, and other forms. We can also computationally obtain numerous types of solitary wave solutions using a variety of approaches. Details concerning their physical behaviour and some of their analytical responses are also provided. These graphs display numerous soliton behaviours of the rsHMBS model to demonstrate how they can be employed to recognise the METF approach physically. For various reasons, it is important to show the solitary wave solutions of the studied rsHMBS model using different graphical forms. The $p(x,t)$ and $q(x,t)$ values of a select few solutions are graphically represented using various diagram types, including profile before revolution shapes, 3D revolving shapes, 2D shapes, contour shapes, and density shapes, to illustrate the solitary wave solutions and enhance our understanding of wave movement and behaviour. Figure 14 displays the profile before revolution shapes, 3D revolving shapes for the solution $p_{11}(\gamma)$ of the rsHMBS model using the values of $T = 3.0$, $A = 2.0$, $E = 0.75$, $D = 2.0$, $C = 1.0$. Figure 15 displays the profile before revolution shapes, 3D revolving shapes for the solution $q_{11}(\gamma)$ of the rsHMBS model using the values of $T = 3.0$, $A = 2.0$, $E = 0.75$, $D = 2.0$, $C = 1.0$, $B = 2.0$, $\delta = 3.0$. Figure 16 displays the profile before revolution shapes, 3D revolving shapes for the solution $p_{24}(\gamma)$ of the rsHMBS model using the values of $T = 3.0$, $A = 2.0$, $E = 1.0$, $D = 5.0$, $C = 1.5$. Figure 17 displays the profile before revolution shapes, 3D revolving shapes for the solution $q_{24}(\gamma)$ of the rsHMBS model using the values of $T = 0.8$, $A = 2.9$, $E = 1.5$, $D = 0.5$, $C = 1.5$, $B = 6.5$, $\delta = 5.5$. Figure 18 displays the profile before revolution shapes, 3D revolving shapes for the solution $p_{33}(\gamma)$ of the rsHMBS model using the values of $T = 0.0$, $A = 2.9$, $E = 1.5$, $D = 1.5$, $C = 7.5$. Figure 19 displays the profile before revolution shapes, 3D revolving shapes for the solution $q_{33}(\gamma)$ of the rsHMBS model using the values of $T = 0.0$, $A = 2.9$, $E = 1.5$, $D = 1.5$, $C = 7.5$, $B = 1.5$, $\delta = 1.5$.

Figure 20 displays the surface and scatter shapes for the solution $p_{11}(\gamma)$ of the rsHMBS model using the values of $T = 0.05$, $A = 0.05$, $E = 0.01$, $D = 0.13$, $C = 0.11$. Figure 21 displays the surface and scatter shapes for the solution $q_{11}(\gamma)$ of the rsHMBS model using the values of $T = 9.0$, $A = 5.0$, $E = 1.0$, $D = 5.0$, $C = 5.0$, $B = 2.0$, $\delta = 2.0$. Figure 22 displays the surface and scatter shapes for the solution $p_{24}(\gamma)$ of the rsHMBS model using the values of $T = -0.05$, $A = 0.05$, $E = 0.01$, $D = 0.13$, $C = 0.11$. Figure 23 displays the surface and scatter shapes for the solution $p_{33}(\gamma)$ of the rsHMBS model using the values of $T = 0.0$, $A = 2.9$, $E = 1.5$, $D = 1.5$, $C = 7.5$. Figure 24 displays the surface and scatter shapes for the solution $q_{33}(\gamma)$ of the rsHMBS model using the values of $T = 0.0$, $A = 2.9$, $E = 1.5$, $D = 1.5$, $C = 7.5$, $B = 1.5$, $\delta = 1.5$.

Figure 25 displays the density and contour shapes for the solution $p_{11}(\gamma)$ of the rsHMBS model using the values of $T = 0.05$, $A = 0.05$, $E = 0.01$, $D = 0.13$, $C = 0.11$. Figure 26 displays the density and contour shapes for the solution $q_{11}(\gamma)$ of the rsHMBS model using the values of $T = 9.0$, $A = 5.0$, $E = 1.0$, $D = 5.0$, $C = 5.0$, $B = 2.0$, $\delta = 2.0$. Figure 27 displays the density and contour shapes for the solution $p_{24}(\gamma)$ of the rsHMBS model using the values of $T = -0.05$, $A = 0.05$, $E = 0.01$, $D = 0.13$, $C = 0.11$. Figure 28 displays the density and contour shapes for the solution $p_{33}(\gamma)$ of the rsHMBS model using the values of $T = 0.0$, $A = 2.9$, $E = 1.5$, $D = 1.5$, $C = 7.5$. Figure 29

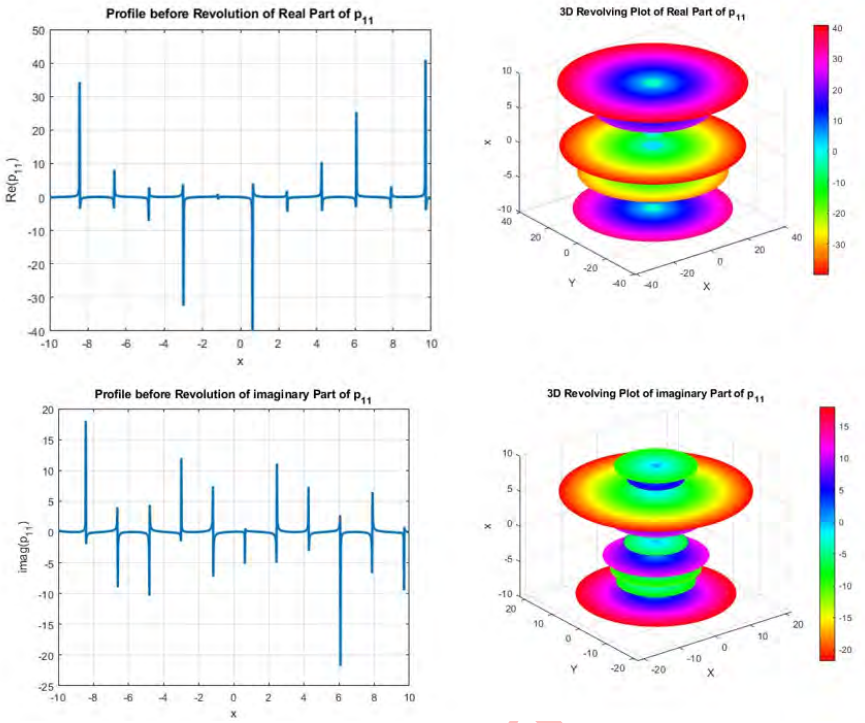

Figure 14. Profile before revolution and 3D revolving plot of the real and imaginary parts of $p_{11}(\gamma)$.

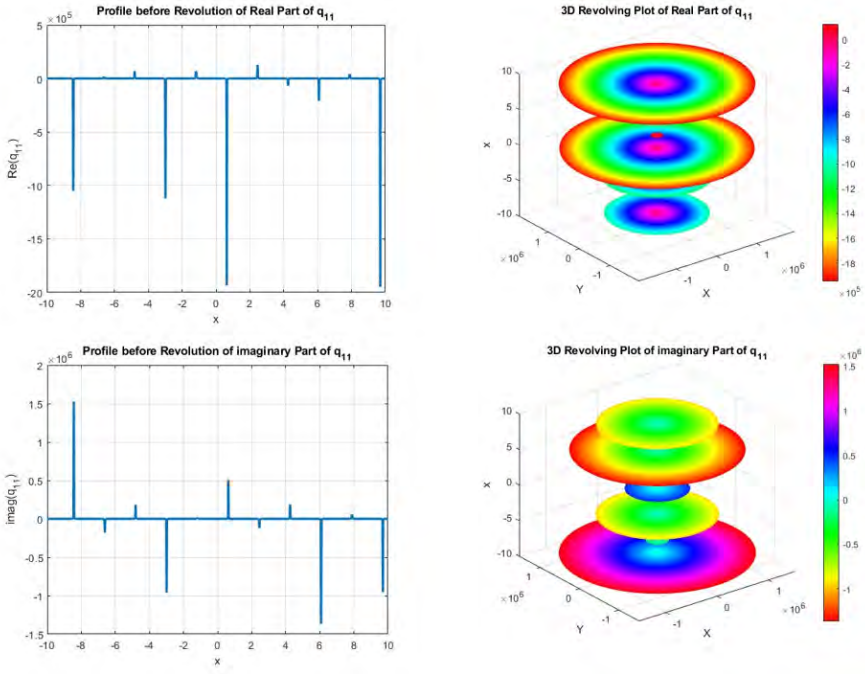

Figure 15. Profile before revolution and 3D revolving plot of the real and imaginary parts of $q_{11}(\gamma)$.

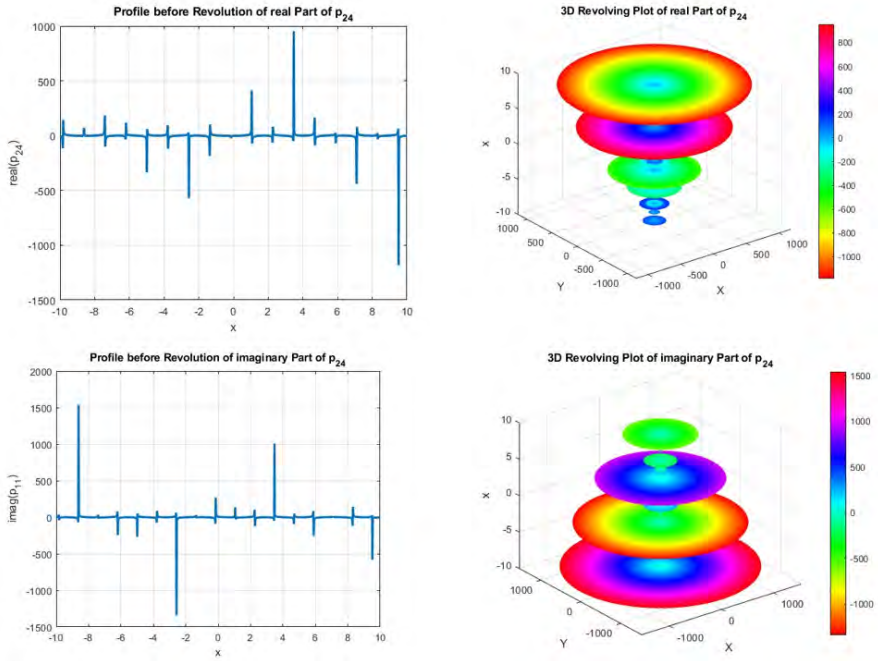

Figure 16. Profile before revolution and 3D revolving plot of the real and imaginary parts of $p_{24}(\gamma)$.

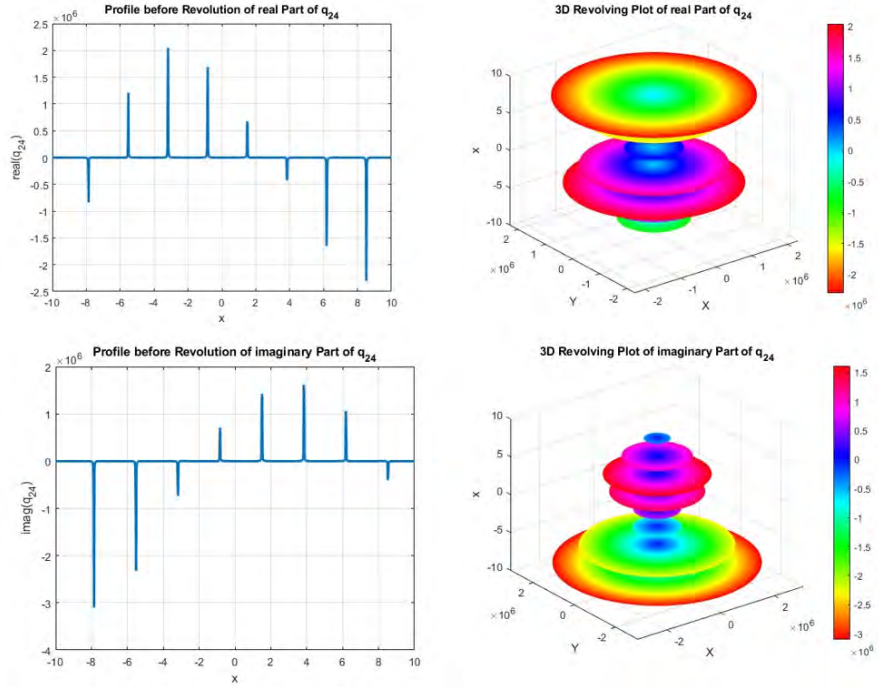

Figure 17. Profile before revolution and 3D revolving plot of the real and imaginary parts of $q_{24}(\gamma)$.

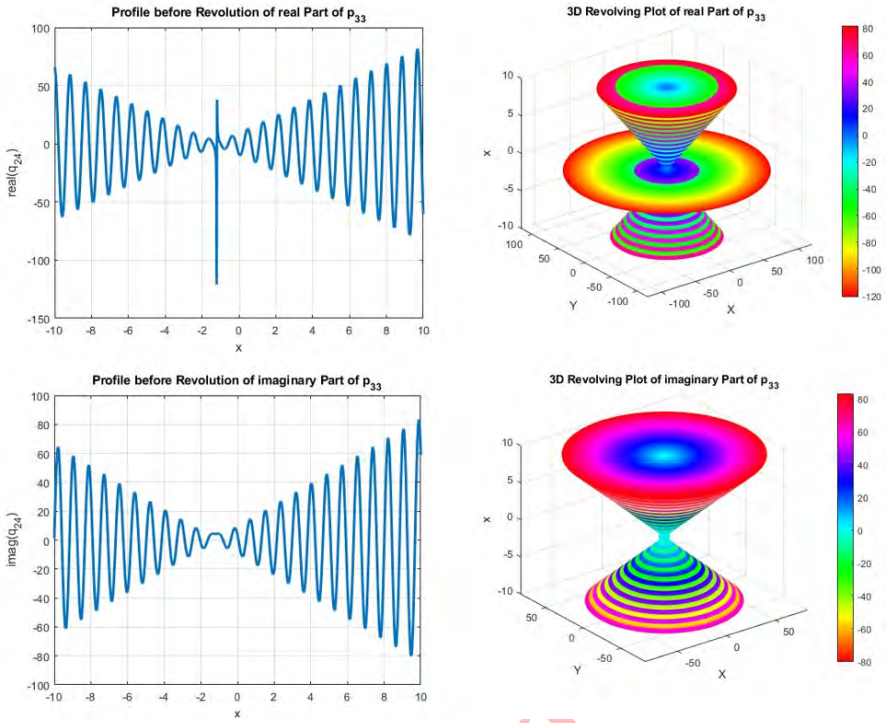

Figure 18. Profile before revolution and 3D revolving plot of the real and imaginary parts of $p_{33}(\gamma)$.

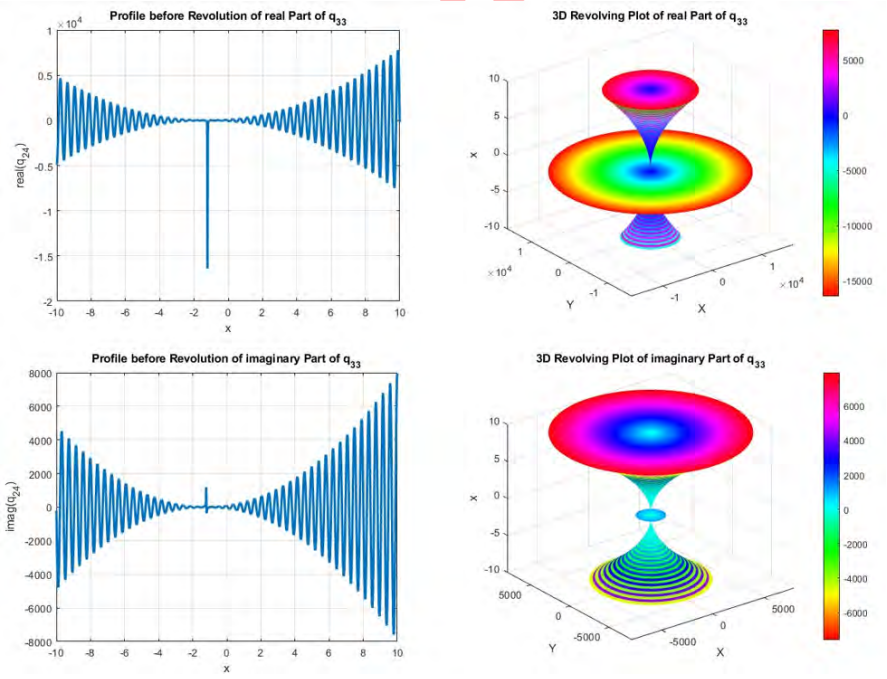

Figure 19. Profile before revolution and 3D revolving plot of the real and imaginary parts of $q_{33}(\gamma)$.

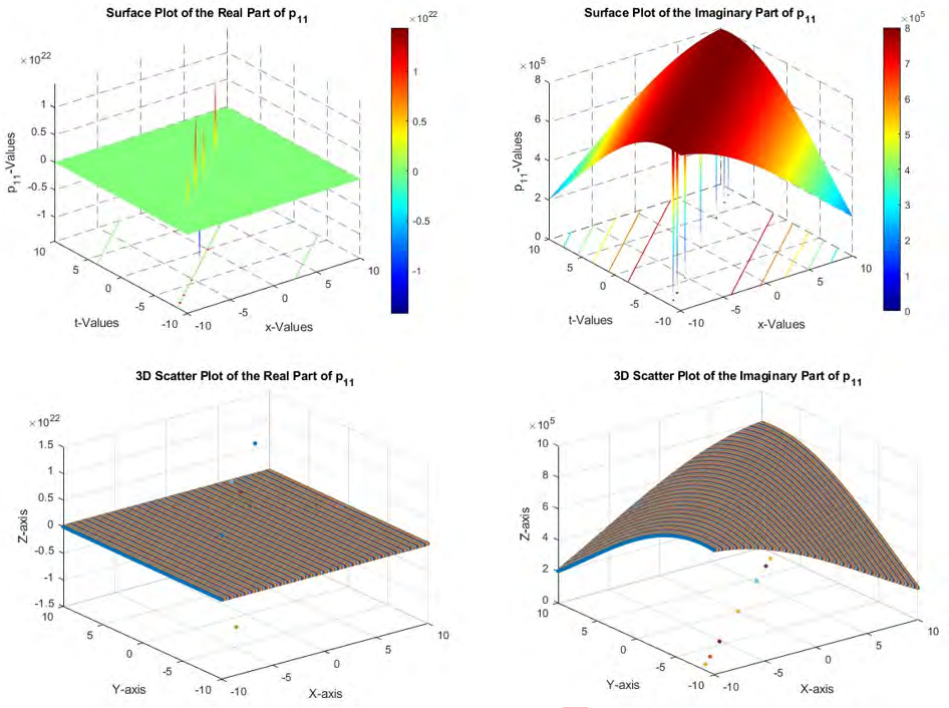

Figure 20. Scatter and surface profiles of the solution $p_{11}(\gamma)$.

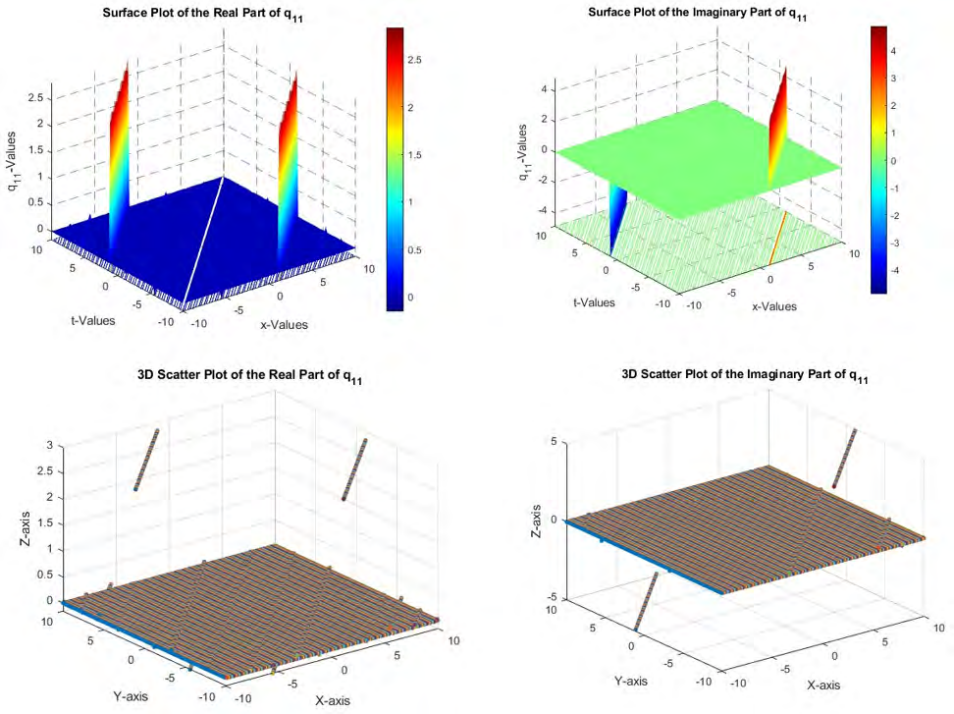

Figure 21. Scatter and surface profiles of the solution $q_{11}(\gamma)$.

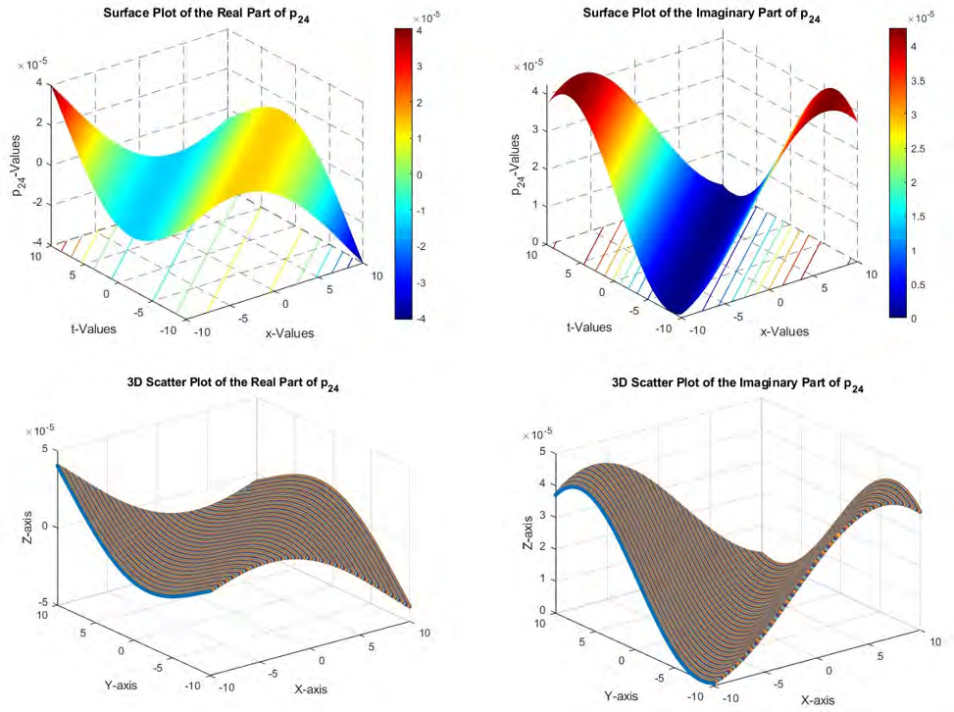

Figure 22. Scatter and surface profiles of the solution $p_{24}(\gamma)$.

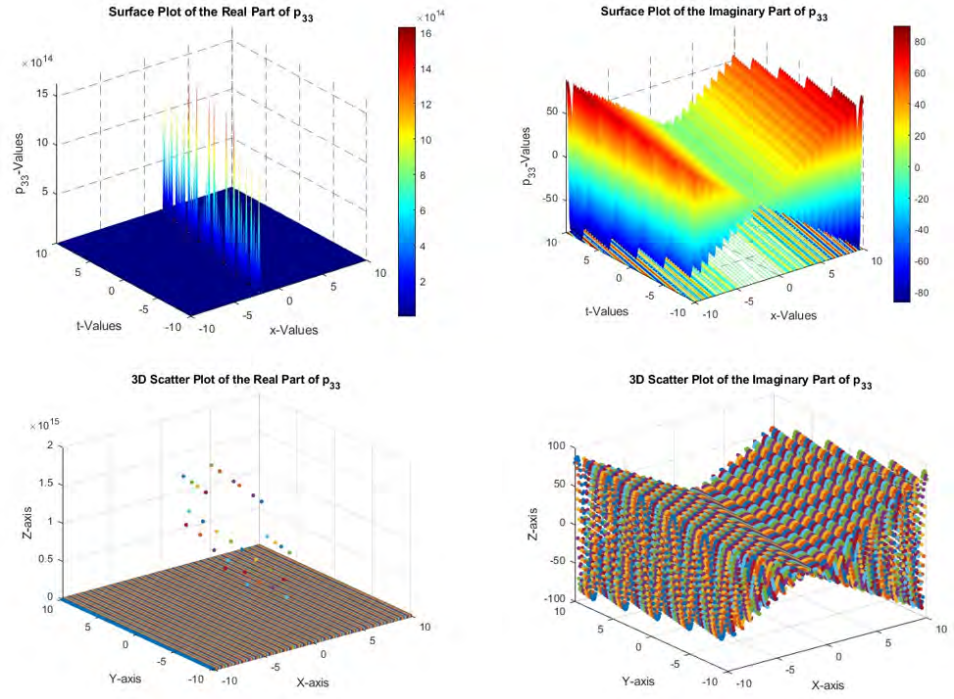

Figure 23. Scatter and surface profiles of the solution $p_{33}(\gamma)$.

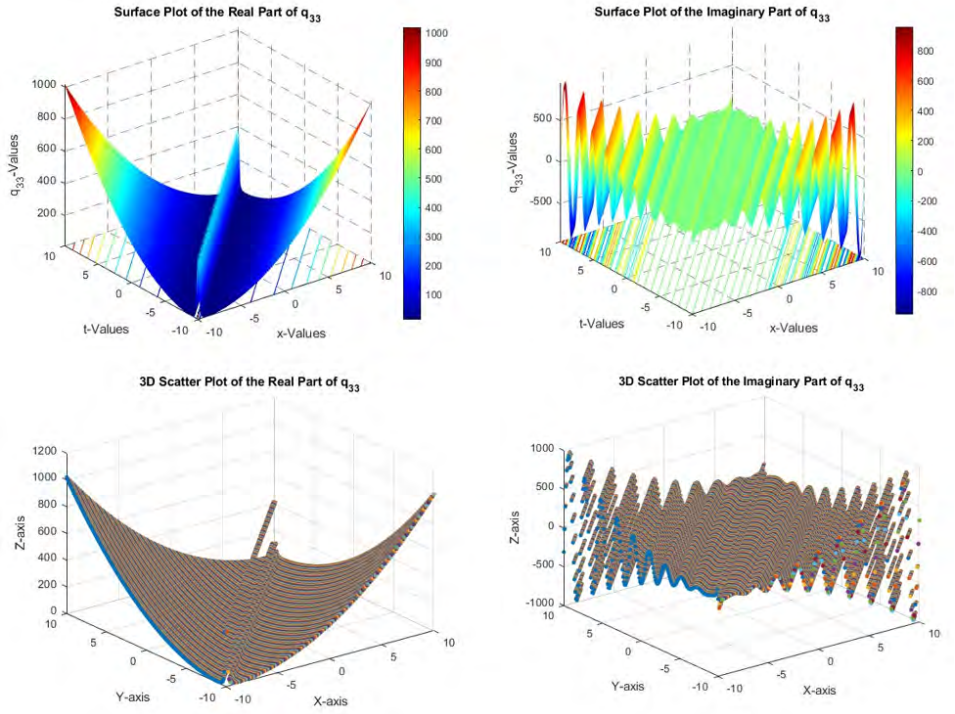

Figure 24. Scatter and surface profiles of the solution $q_{33}(\gamma)$.

displays the density and contour shapes for the solution $q_{33}(\gamma)$ of the rsHMBS model using the values of $T = 0.0$, $A = 2.9$, $E = 1.5$, $D = 1.5$, $C = 7.5$, $B = 1.5$, $\delta = 1.5$.

Figure 30(a) displays the 2D shapes for the solution $p_{11}(\gamma)$ of the rsHMBS model using the values of $T = 0.05$, $A = 0.05$, $E = 0.01$, $D = 0.13$, $C = 0.11$ with $t = [1, 10, 20, 100]$. Figure 30(b) displays the 2D shapes for the solution $q_{11}(\gamma)$ of the rsHMBS model using the values of $T = 9.0$, $A = 5.0$, $E = 1.0$, $D = 2.0$, $C = 5.0$, $B = 2.0$, $\delta = 3.0$ with $t = [1, 10, 20, 100]$. Figure 30(c) displays the 2D shapes for the solution $p_{24}(\gamma)$ of the rsHMBS model using the values of $T = -0.05$, $A = 0.05$, $E = 0.01$, $D = 0.13$, $C = 0.11$ with $t = [1, 10, 20, 100]$. Figure 30(d) displays the 2D shapes for the solution $q_{24}(\gamma)$ of the rsHMBS model using the values of $T = -9.0$, $A = 5.0$, $E = 1.0$, $D = 5.0$, $C = 5.0$, $B = 2.0$, $\delta = 2.0$ with $t = [1, 10, 20, 100]$. Figure 30(e) displays the 2D shapes for the solution $p_{33}(\gamma)$ of the rsHMBS model using the values of $T = 0.0$, $A = 2.9$, $E = 1.5$, $D = 1.5$, $C = 7.5$ with $t = [1, 10, 20, 100]$. Figure 30(f) displays the 2D shapes for the solution $q_{33}(\gamma)$ of the rsHMBS model using the values of $T = 0.0$, $A = 2.9$, $E = 1.5$, $D = 1.5$, $C = 7.5$, $B = 1.5$, $\delta = 1.5$ with $t = [1, 10, 20, 100]$.

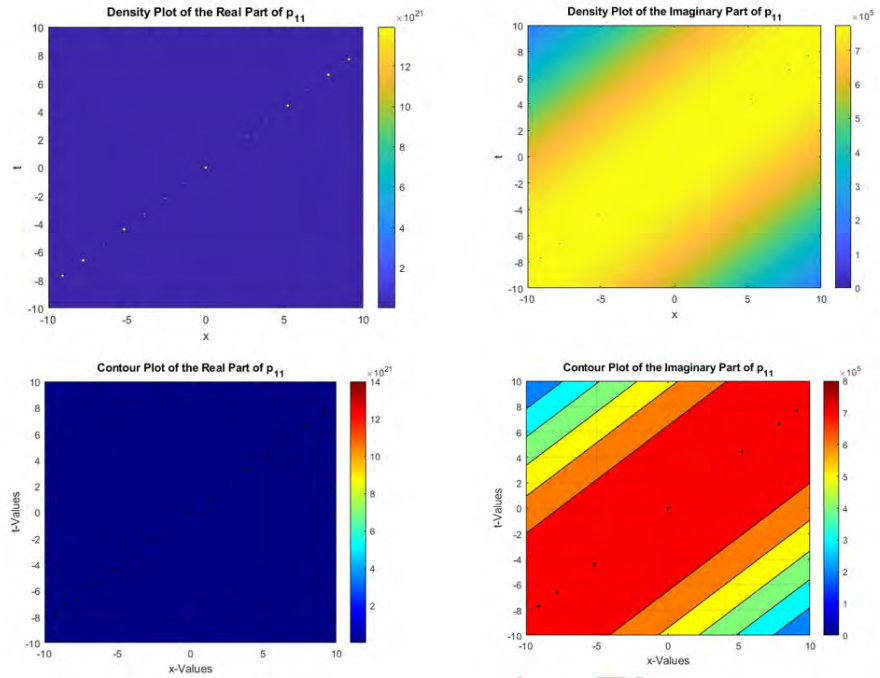

Figure 25. Contour and density profiles of the solution $p_{11}(\gamma)$.

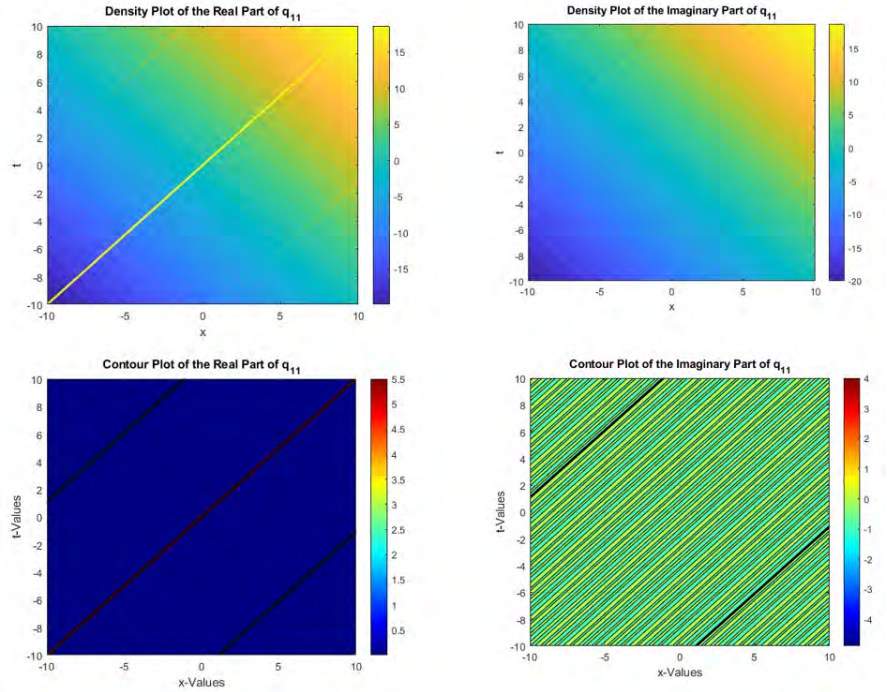

Figure 26. Contour and density profiles of the solution $q_{11}(\gamma)$.

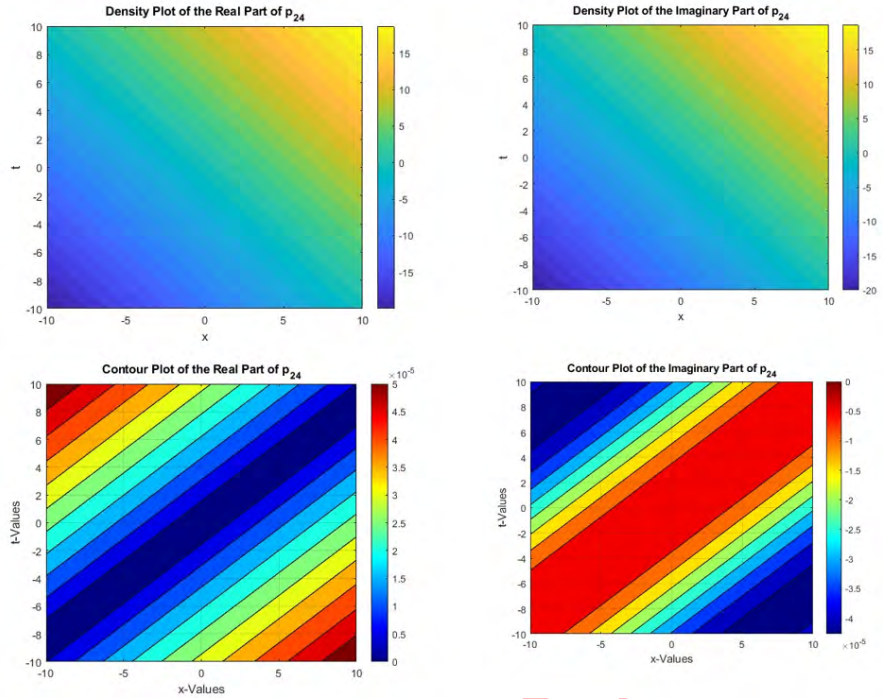

Figure 27. Contour and density profiles of the solution $p_{24}(\gamma)$.

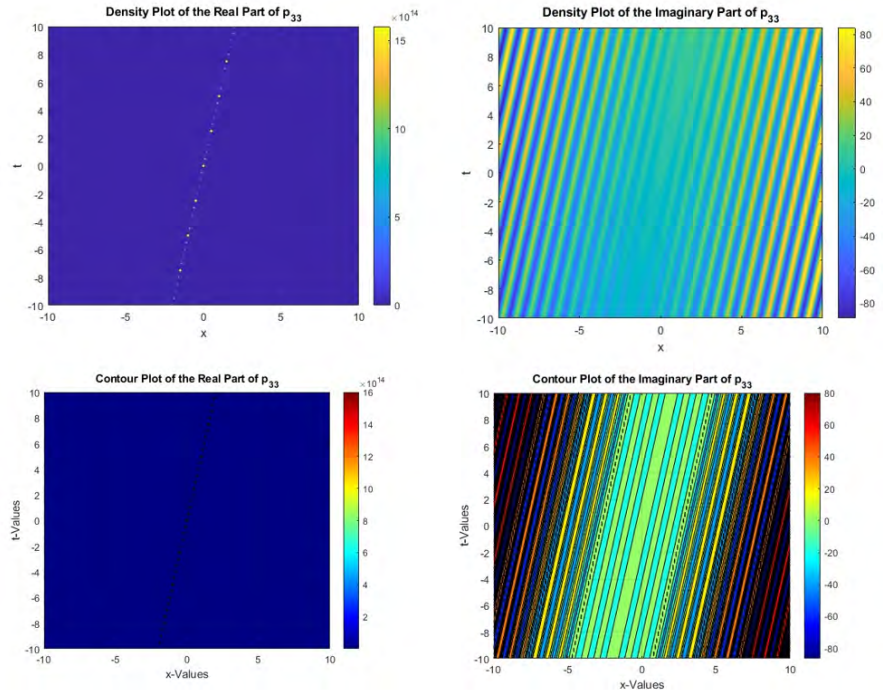

Figure 28. Contour and density profiles of the solution $p_{33}(\gamma)$.

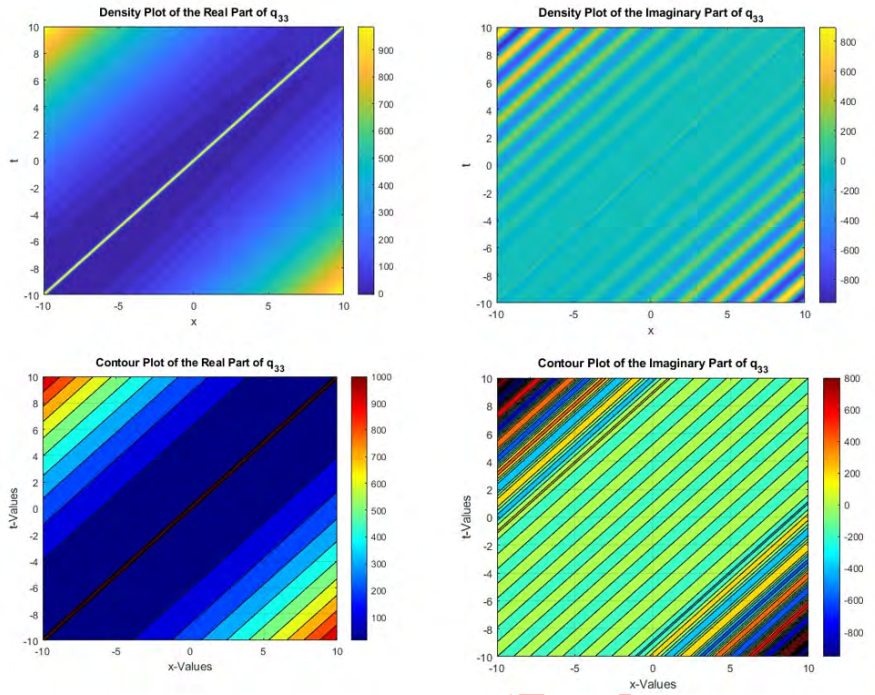

Figure 29. Contour and density profiles of the solution $q_{33}(\gamma)$.

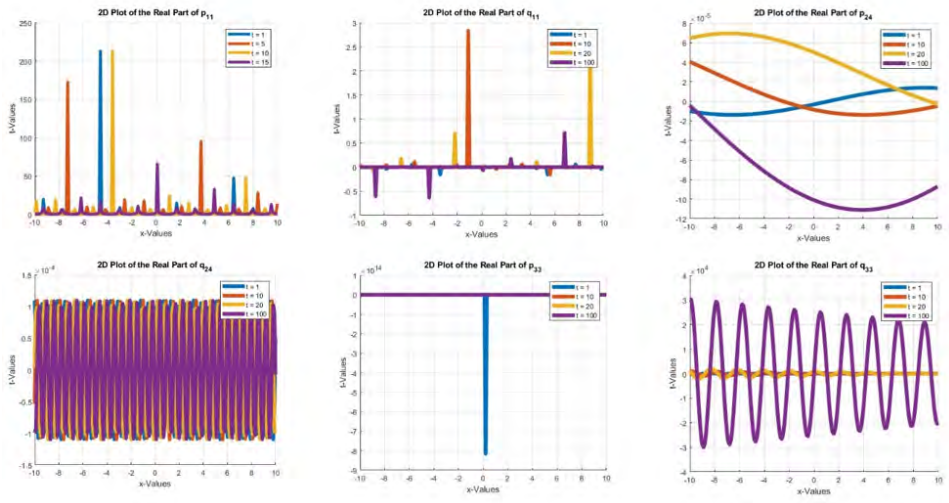

Figure 30. 2D profiles of the solutions $p_{11}(\gamma)$, $p_{24}(\gamma)$, $p_{33}(\gamma)$, $q_{11}(\gamma)$, $q_{24}(\gamma)$, and $q_{33}(\gamma)$.

These four varieties of diagrams are crucial for exploring NLEEs for the reason that they generate it simpler to comprehend, picture, and analyses soliton solution presentations. While scientifically precise, theoretically produced soliton solutions, for example bell-shaped solitons, multiple solitons, bright soliton, V-shaped solitons, singular periodic solitons, compaction solitons, and peakons that requirement watchful deliberation for their probable requests in erbium-doped fibre systems. Bright solitons that comparable to optical pulses that assert their truthfulness and

energy over continued propagation lengths, appear in inconsistent dispersion managements. Anti-kink solitons, singular solitons, singular kinks, quasiperiodic structures, periodic structures, and other forms that manifest as patches of reduced intensity on a steady light background are often linked to typical dispersion conditions. Singular solitons are characterised by abrupt peaks or singularities in amplitude; they might be a sign of localised energy accumulation in fibre systems or a condition that causes nonlinear instability. The theory is easier to relate to when one understands the results of solitons in terms of experimentally observable properties such as pulse width, peak amplitude, energy content, and propagation speed. Results from experiments offer useful recommendations for practical applications. By investigating the effects of input power on doping concentrations in erbium-doped fibres, researchers may experimentally demonstrate stationary soliton behaviour. The significance of the proposed model in the field of nonlinear photonics and its applicability to fibre optics are further highlighted by offering commentary on how it might be used in experimental settings using femtosecond and picosecond pulse production, as well as ultrafast optical diagnostics. The close connection between theoretical concepts and experimental measurements significantly enhances the practical effectiveness of this research.

5. Conclusion

A dynamical systems framework was generated in the current study, focusing on bifurcation analysis, chaotic and quasi-periodic behaviour, sensitivity tests, and novel soliton solutions for the rsHMB equation using the METF approach. To understand the planar dynamical system and demonstrate its reliance on physical characteristics, such as quasiperiodic and sensitivity analysis, we employ bifurcation and chaos theories. A comprehensive stability analysis, guided by bifurcation theory, revealed the system's dynamic behaviour under different parameter regimes. Hamiltonian projections were also provided to more deeply explain how trajectories spread out in the neighbourhoods of equilibrium points. This resulted in revealing the complex dynamics of the dynamical response. These novel findings provide fresh perspectives on the dynamics of wave motion in mathematical models to understand the stability and transitions of nonlinear pulse dynamics in fiber lasers. These experiments exhibits when stable solitons create, when solitons destabilize, and how minimum varies in parameters affect pulse propagation. To visualize the significance of these nonlinear dynamical outcomes as 2D and 3D phase portraits, sensitivity behaviours, time series, contour maps, density diagrams, and surface phases for different initial conditions. The findings will contribute to a better understanding of the physical situation of nonlinear wave propagation in other physical situations, such as controlling ultrafast laser pulses, designing stable high-speed fiber optic communication, enabling secure chaos-based data transfer, improving medical laser imaging, and advancing magnetic storage technologies. Finally, we found exact optical soliton solutions for rsHMBS in this work, which can be used to transmit femtosecond pulses in an erbium-doped fiber. The METF approach has been successfully applied to construct several solutions, including compaction solitons, singular periodic solitons, V-shape solitons, bell-shaped solitons, and anti-kink solitons. We use symbolic computers to handle nonlinear wave issues in a variety of domains, including engineering and mathematical physics. Furthermore, these solutions might be helpful in every area of mathematical physics and engineering. The findings support the success of the METF approach in producing explicit solutions to NLPDEs. The rsHMB equation equation's bifurcation dynamics, sensitivity characteristics, and soliton structures are successfully investigated in this paper, although there are still a number of restrictions and difficulties. The complexity of real optical systems, including higher-dimensional disturbances, inhomogeneous media, and external noise effects, may not be well captured by the current study, which mainly concentrates on one-dimensional formulations and idealised parameter conditions. Furthermore, the METF method may not be as applicable to more complex or stochastic versions of the rsHMB model, despite its strength in obtaining precise analytical solutions. When working with highly sensitive or chaotic regimes, numerical simulations based on deterministic techniques like Runge-Kutta also encounter computing limitations. Future research could develop hybrid analytical–computational frameworks with machine learning or neural network-based algorithms to handle high-dimensional or non-integrable expansions of the rsHMB issue. Examining fractional-order and nonlocal versions of the model may help us better understand long-memory effects and complex wave interactions. Investigating optical implementation and experimental validation of the theoretical results in erbium-doped fibre systems would also increase the practical impact. These avenues could enhance our comprehension of nonlinear wave dynamics and broaden the application of soliton-based technologies in modern photonics.

Acknowledgment

Funding: There is no funding for this research.
Data Availabilit: Not applicable.
Conflict of Interest: No potential conflict of interest was reported by the authors.

References

[1] S. Akram and M. U. Rahman, *Exploring nonlinear dynamics and soliton structures in the Spin Reduced Hirota-Maxwell-Bloch system via Atangana's conformable operator*, Chinese Journal of Physics, *97* (2025), 1514–1538.
[2] M. N. Alam, M. Iqbal, M. Hassan, M. F. A. Asad, M. S. Hossain, and C. Tunç, *Bifurcation, phase plane analysis and exact soliton solutions in the nonlinear Schrodinger equation with Atangana's conformable derivative*, Chaos, Solitons and Fractals, *182* (2024), 114724.
[3] M. Z. Baber, M. W. Yasin, N. Ahmed, S. M. Ali, and M. Ali, *Dynamical analysis and optical soliton wave profiles to GRIN multimode optical fiber under the effect of noise*, Nonlinear Dynamics, *112* (2024), 20183–20198.
[4] B. Ceesay, M. W. Yasin, N. Ahmed, M. Z. Baber, and E. Bittaye, *Revealing homoclinic breather waves, periodic lump waves and other waves forms of an integrable reduced spin Hirota-Maxwell-Bloch system*, Scientific Reports, *15* (2025), 19880.
[5] X. Q. Cui, B. J. Zhang, and X. Y. Wen, *Bright-dark soliton solutions and their elastic interaction analysis for a reduced integrable spin Hirota–Maxwell–Bloch equation*, Fractal and Fractional, *82* (2023), 94-104.
[6] J. A. Haider, S. Ahmad, K. A. Gepreel, and R. A. Rahman, *Multifaceted simulation: Finite volume and finite element modeling of blood flow in multiple stenosed arteries*, Modern Physics Letters B, *39* (2025), 2450395.
[7] J. A. Haider and S. Ahmad, *Dynamics of the Rabinowitsch fluid in a reduced form of elliptic duct using finite volume method*, International Journal of Modern Physics B, *36* (2022), 2250217.
[8] J. A. Haider, S. Ahmad, H. A. Ghazwani, M. Hussien, M. Y. Almusawa, and E. A. Az-Zo'bi, *Results validation by using finite volume method for the blood flow with magnetohydrodynamics and hybrid nanofluids*, Modern Physics Letters B, *38* (2024), 2450208.
[9] J. A. Haider, S. Ahmad, and S. Nadeem, *Mathematical modeling of electroosmotic flow and thermal transport in stenotic tapered arteries using finite difference method*, Modern Physics Letters B, *39* (2025), 2550117.
[10] Z. R. Liu and J. B. Li, *Bifurcation of solitary waves and domain wall waves for KdV-like equation with higher order nonlinearity*, Int. J. Bifurc. Chaos, *12* (2002), 397–407.
[11] A. A. Mahmud, *Considerable traveling wave solutions of the generalized Hietarinta-type equation*, International Journal of Mathematics and Computer in Engineering, *3* (2025), 185-200.
[12] S. Manukure and T. Booker, *A short overview of solitons and applications*, Partial Differential Equations in Applied Mathematics, *4* (2021), 100140.
[13] H. Song and B. Ren, *General rogue waves and modulation instability of the generalized coupled nonlinear Schrodinger system in optical pulses*, Chaos, *35* (2025), 033121.
[14] A. Taskeen, M. O. Ahmed, M. Z. Baber, B. Ceesay, and N. Ahmed, *Bifurcation, chaotic, sensitivity analysis, and optical soliton profiles for the Spin–Hirota–Maxwell–Bloch equation erbium-doped fiber*, Advances in Mathematical Physics, *2025* (2025), 7157902.
[15] S. Turitsyn and A. Mikhailov, *Applications of solitons, Scattering*, Elsevier, *2002* (2002), 1741-1753.
[16] M. S. Ullah, H. O. Roshid, and M. Z. Ali, *Bifurcation analysis and new waveforms to the first fractional WBBM equation*, Scientific Reports, *14* (2024), 11907.
[17] T. Usman, I. Hossain, M. S. Ullah, and M. M. Hasan, *Soliton, multistability and chaotic dynamics of the higher order nonlinear Schrodinger equation*, Chaos, *35* (2025), 04314.
[18] J. Wang, Y. Liu, L. Yan, K. Han, L. Feng, and R. Zhang, *Fractional sub-equation neural networks (fSENNs) method for exact solutions of space–time fractional partial differential equations*, Chaos, *35* (2025), 043110.
[19] K. L. Wang, *Novel solitary wave and periodic solutions for the nonlinear Kaup-Newell equation in optical fibers*, Opt. Quantum Electron, *56* (2024), 514.
[20] K. L. Wang, *New solitary wave solutions and dynamical behaviors of the nonlinear fractional Zakharov system*, Qual. Theory Dyn. Syst., *23* (2024), 98.

[21] X. R. Xie and R. F. Zhang, *Neural network-based symbolic calculation approach for solving the Korteweg–de Vries equation*, Chaos, Solitons and Fractals, *194* (2025), 116232.
[22] Y. S. Xue, B. Tian, W. B. Ai, F. H. Qi, R. Guo, and B. Qin, *Soliton interactions in a generalized inhomogeneous coupled Hirota–Maxwell–Bloch system*, Nonlinear Dynamics, *67* (2012), 2799-2806.
[23] K. Yesmakhanova, G. Shaikhova, G. Bekova, and R. Myrzakulov, *Exact solutions for (2+1)-dimensional Hirota-Maxwell-Bloch system*, AIP Conference Proceedings, *1880* (2017), 060022.
[24] S. Yuan, Y. Liu, L. Yan, R. Zhang, and S. Wu, *Neural Networks-Based Analytical Solver for Exact Solutions of Fractional Partial Differential Equations*, Fractal and Fractional, *9* (2025), 541.
[25] N. J. Zabusky and M. A. Porter, *Soliton*, Scholarpedia, *5* (2010), 2068.
[26] R. F. Zhang and S. Bilige, *Bilinear neural network method to obtain the exact analytical solutions of nonlinear partial differential equations and its application to p-gBKP equation*, Nonlinear Dyn., *95* (2019), 3041–3048.
[27] H. Zhang, R. Zhang , and Q. Liu, *A Novel Multi-Modal Neurosymbolic Reasoning Intelligent Algorithm for BLMP Equation*, Nonlinear Dyn., *42* (2025), 100002.
[28] R. F. Zhang and M. C. Li, *Bilinear residual network method for solving the exactly explicit solutions of nonlinear evolution equations*, Nonlinear Dyn., *108* (2022), 521–531.